Technische Universität München
Fakultät für Physik

**Abschlussarbeit im Masterstudiengang Physik (Kern-, Teilchen- und Astrophysik)**

# Sensitivity Studies for KATRIN and Investigation of the Column Density with First KATRIN Data

**Sensitivitätsstudien für KATRIN und Untersuchung der Säulendichte mit ersten KATRIN Daten**

Dominik Raphael Fuchs

23.10.2018

Erstgutachter (Themensteller): Prof. Dr. S. Mertens

# Contents

# Contents

iv

# Abstract

The KArlsruhe TRItium Neutrino (KATRIN) experiment is designed to determine the effective electron anti-neutrino mass with a sensitivity of 200 meV/$c^2$ (90% C.L.) by the investigation of the kinematics of tritium beta decay in a direct and model independent way.

The two main goals of this thesis are to provide an overview of systematic effects and their importance at different stages of the KATRIN experiment. The second part focuses on the analysis of the data obtained during the First Tritium Campaign in May and June 2018. The analysis performed in this work focuses on a determination of the column density, an important model parameter, from the data.

# Chapter 1

# Introduction

Since the neutrino was first postulated by Pauli in 1930 [1] and was detected for the first time in 1953 by Reines and Cowan [2] it has always been an extremely intriguing object of research. Over the course of the last decades the neutrino sector became a very active field of physics and many properties of the neutrinos have been studied in detail.

Neutrinos are electrically neutral and couple only to the weak interaction, which makes their detection rather difficult. The known active neutrinos come in three different flavors. One of their key characteristics is their ability to change flavor between creation and detection. Those neutrino oscillations were experimentally verified by the Super-Kamiokande experiment [3] and the SNO experiment [4]. The existence of such oscillations however requires the neutrinos to have a non-vanishing mass, replacing the previous assumption of neutrinos beeing massless particles.

Various oscillation experiments have determined the mass differences of the three mass eigenstates of the neutrinos with high precision. However the total mass scale is inaccessible by such experiments. Several different methods are currently used by many experiments to investigate this open question. Currently the best direct limits come from the Mainz neutrino mass experiment [5] and the Troitsk nu-mass experiment [6] as well as a combined analysis [7] setting an upper limit of $m_\nu < 2.0$ eV (95 % C.L.).

The KATRIN experiment will improve this limit by one order of magnitude, targeting a sensitivity of $m_\nu < 0.2$ eV (90% C.L.) after a runtime of three years [8].

Chapter 2 will give a quick overview of neutrino physics, focusing on neutrino oscillations and different methods to obtain the total mass scale. The third chapter

introduces the KATRIN experiment with all its components and a brief explanation of its measurement principle as well as a short introduction of the analysis software tools used for this thesis and a short description of their underlying model. The sensitivity studies in chapter 4 investigate the relevance of certain systematic uncertainties during different stages of the KATRIN experiment. The subsequent chapter presents fit results of First tritium data and their evolution over the time of the first data taking phase. Chapter 6 will give a deeper look into the determination of the column density of the KATRIN source. Finally this thesis will end in a Conclusion and an Outlook.

# Chapter 2

# Neutrino physics

In the Standard Model neutrinos are part of the three lepton generations. Every generation contains one electrically charged lepton and an electrically neutral corresponding neutrino. There are electron-, muon- and tau-neutrinos. Following a recap of their postulation and discovery a short introduction into neutrino oscillations is given. As a last point of this chapter some methods for determining the total neutrino mass are presented.

## 2.1 Discovery of Neutrinos

As physicists started to look deeper into radioactive processes they soon found some oddities connected with the $\beta$-decay, specifically concerning its spectral shape. At that time the only measurable particles of this process were the decaying nucleus, its daughter nucleus and the electron, making it a two-body decay. In that case though the expected electron energy should, equally to the $\alpha$- and $\gamma$-decay, be monoenergetic to comply with the rules of energy and momentum conservation. Contrary to this expectation the $\beta$-spectrum turned out to be continuous [9]. Furthermore the description of the $\beta$-decay as a two-body decay led to violations of angular momentum conservation.

Pauli solved all those problems by introducing a new neutral spin 1/2-particle [1], fulfilling all the necessary properties. This particle, later labeled as neutrino by

Enrico Fermi, shared the decay energy with the electron, explaining the continuous spectrum.

$$n \rightarrow p + e^- + \bar{\nu}_e$$
$$p \rightarrow n + e^+ + \nu_e$$

(2.1)

In the $\beta^-$-decay there has to occur an anti-neutrino $\bar{\nu}_e$ for lepton number conservation. In contrast the $\beta^+$-decay, which is energetically not allowed outside of a nucleus, produces a neutrino.

Enrico Fermi delivered the first full theory of $\beta$-decay in 1934 [10] which is still valid within low energy limits. This theory was the foundation of the modern theory of weak interaction.

In consequence of their color or electrical neutrality the proof of the neutrino's existence was not an easy task. The predicted cross section of about $\sigma < 10^{-44}$ cm$^2$ [11] that prevented the neutrino's discovery up to that time was further on a challenging endeavour for physicists.

The first neutrino was detected over twenty years after its postulation by Reines and Cowan at the Savannah River Experiment [12]. They made use of the inverse $\beta$-decay:

$$\bar{\nu}_e + p \rightarrow e^+ + n$$

(2.2)

To get enough events despite the extremely small cross section they placed their detector close to one of the Savannah River Plant reactors which was used as a strong electron antineutrino source. The detector was composed of two layers of water with cadmium chloride and three layers of liquid scintillator. The incoming antineutrinos react with the protons of the hydrogen. The resulting positron almost immediately annihilates with an electron into two 511 keV photons, while the neutron moderates for a few µs until it is captured by one of the cadmium nuclei. The excited cadmium nucleus in turn deexcites releasing one or several gamma rays with 9 MeV in total [12]. This characteristic signal was very convenient to discriminate it from background. The measured cross section was in good agreement with the predictions.

In 1962 the muon neutrino $\nu_\mu$ was found at the Brookhaven National Laboratory [13]. When the tau lepton $\tau$ was discovered in 1975 it was expected that a corresponding neutrino should also exist. It took until 2001 for the tau neutrino $\nu_\tau$ to be finally detected by the DONUT experiment [14], completing the picture of the three lepton generations in the Standard Model. From the beginning it was already clear that the neutrino mass must be very small, if not even zero and so in the Standard Model the neutrinos are considered as massless particles. However the discovery of neutrino oscillations as explained in 2.2 undeniably showed that neutrinos must have a non-vanishing mass.

## 2.2 Neutrino oscillations

The first hint that led physicists into considering oscillating neutrinos was the so called "solar neutrino problem". The Homestake experiment was the first one to reveal this problem, followed by several others. The experiment's goal was to verify the theoretically predicted neutrino flux from the sun, but instead found the rate to be too low, measuring only about 1/3 of the expected flux [15]. Rather soon it became clear that no modifications of the solar model could explain those results, leading the scientists to the possible explanation that the neutrinos must have changed their flavour during propagation.

The neutrinos are created via the weak interaction as one of the flavour eigenstates $|\nu_\alpha\rangle$ with $\alpha = e$, $\mu$, $\tau$. Those flavour eigenstates are in turn superpositions of the three mass eigenstates $|\nu_i\rangle$ with $i = 1, 2, 3$, related via the unitary PMNS (Pontecorvo [16][17][18], Maki, Nakagawa and Sakata [19]) matrix U:

$$\begin{aligned}
|\nu_\alpha\rangle &= \sum_i U_{\alpha i}^* |\nu_i\rangle \\
|\nu_i\rangle &= \sum_\alpha U_{\alpha i} |\nu_\alpha\rangle
\end{aligned}$$

(2.3)

$U_{\alpha i}$ are the matrix elements of the neutrino mixing matrix. For the three active neutrinos the PMNS matrix can be parametrized as follows:

$$
\begin{aligned}
U &= \begin{pmatrix} U_{e1} & U_{e2} & U_{e3} \\ U_{\mu 1} & U_{\mu 2} & U_{\mu 3} \\ U_{\tau 1} & U_{\tau 2} & U_{\tau 3} \end{pmatrix} \\
&= \begin{pmatrix} 1 & 0 & 0 \\ 0 & c_{23} & s_{23} \\ 0 & -s_{23} & c_{23} \end{pmatrix} \times \begin{pmatrix} c_{13} & 0 & s_{13} \cdot e^{-i\delta} \\ 0 & 1 & 0 \\ -s_{13} \cdot e^{-i\delta} & 0 & c_{13} \end{pmatrix} \times \begin{pmatrix} c_{12} & s_{12} & 0 \\ -s_{12} & c_{12} & 0 \\ 0 & 0 & 1 \end{pmatrix} \\
&\times \begin{pmatrix} 1 & 0 & 0 \\ 0 & e^{i\alpha_1} & 0 \\ 0 & 0 & e^{i\alpha_2} \end{pmatrix}
\end{aligned}
\tag{2.4}
$$

With the mixing angles $s_{ij} = \sin \theta_{ij}$ and $c_{ij} = \cos \theta_{ij}$ and the CP-violating phases $\delta$ (Dirac phase) and $\alpha_1$, $\alpha_2$ (Majorana phases). With this parametrization the matrix can be split up in several matrices each containing one of the mixing angles.

For times $t > 0$, equation 2.3 has to be modified by the time evolution operator of the mass eigenstates:

$$
|\nu_\alpha (t > 0)\rangle = \sum_i U_{\alpha i}^* \, e^{-iE_i t} \, |\nu_i\rangle
\tag{2.5}
$$

As long as at least two of the $m_i$ are different, the time evolution operator will behave differently for those mass eigenstates, causing the neutrinos to change their flavour over time. From this the probability to detect a neutrino of a certain flavour which was created as a different flavour can be calculated. For simplicity only the formula for a two flavour scenario is shown here:

$$
P_{\nu_\alpha \to \nu_\beta}(L, E) = \sin^2(2\theta_{ij}) \, \sin^2 \left( \frac{\Delta m_{ij}^2 \cdot L}{4 \cdot E} \right)
\tag{2.6}
$$

From this equation it can be seen that with a known distance $L$ of the detector to the neutrino source and a known neutrino energy $E$ the mass square differences $\Delta m_{ij}^2 = m_i^2 - m_j^2$, defining the frequency of the oscillations, and the mixing angles $\theta_{ij}$, defining the amplitude, can be measured.

The neutrino oscillations were eventually verified by several experiments among which two of the most important ones are the Sudbury Neutrino Observatory (SNO) experiment and the Super-Kamiokande experiment. In 2001 the SNO experiment, which was sensitive to all neutrino flavours, was measuring solar neutrinos and found evidence for neutrino oscillations [20]. Giving a mass square difference of the oscillations between electron and muon neutrinos, also called solar neutrino oscillations, of $\Delta m_{12}^2 = \Delta m_{solar}^2 \simeq 7.37 \cdot 10^{-5}$ eV$^2$ [21]. The Super-Kamiokande experiment was the first one to give clear evidence for neutrino oscillations in 1998 [3]. Giving a mass square difference of the muon and tau neutrino oscillations, also called atmospheric neutrino oscillations, of $|\Delta m_{23}^2| = |\Delta m_{atmos}^2| \simeq 2.55 \cdot 10^{-3}$ eV$^2$ [21].

As can be seen above the neutrino oscillation experiments only allow for mass square differences to be measured, not the absolute mass scale of the neutrinos. In principle there are three possibilities for the neutrino mass ordering. First of all the quasi degenerate case, where $m_1 \approx m_2 \approx m_3 \approx m_0$, respectively $\Delta m^2 \ll m_i^2$. The hierarchical case ($\Delta m^2 \approx m_i^2$) can be split up into two scenarios: The normal hierarchy ($m_1 < m_2 \ll m_3$) or the inverted hierarchy ($m_3 \ll m_1 < m_2$). To determine the absolute neutrino mass scale different experimental strategies are needed, introduced in 2.3.

## 2.3 Methods for neutrino mass determination

The neutrinos absolute mass is a crucial parameter for particle and astroparticle physics as well as cosmology. The neutrinos have impact on many processes including primordial nucleosynthesis and the structure formation in the universe and even help to predict the further evolution of the universe. Those were just some of the many reasons why it is important to find the neutrino mass. As already mentioned, oscillation experiments can not get access to the absolute mass but rather mass square differences, leading experimentalists to come up with alternative ideas.

### 2.3.1 Neutrino mass limits from cosmology

The deduction of the neutrino mass from cosmology or astro(particle) physics has the downside of being model dependent. According to which model is being used, the result of the neutrino mass can alter significantly. Also the uncertainty of other

parameters of the model, which might be correlated with the neutrino mass can enlarge the uncertainty of the result. The standard cosmological model is the $\Lambda$CDM (Lambda cold dark matter) model, with $\Lambda$ being the cosmological constant.

To get a limit on the neutrino mass, the neutrino influence on processes like structure formation or supernovae explosions as well as the cosmic microwave background (CMB) are exploited. The experiments are typically sensitive to the sum of the neutrino mass eigenstates $m_{\nu_{cosm}} = \sum_i m_i$.

A more detailed description and current results can be found in [22] [21]. Usually several data sets are combined to avoid correlations or constrain certain parameters. Depending on the model and the combined data sets, the results range from $\sum_i m_i < 0.12$ eV to $\sum_i m_i < 0.73$ eV (95 % C.L.) [21].

### 2.3.2 Neutrino mass limits from neutrinoless double beta decay

The double beta decay ($2\nu\beta\beta$) can be described as a simultaneous decay of two neutrons to two protons under radiation of two electrons and two neutrinos in the same nucleus.

$$2n \rightarrow 2p + 2e^- + 2\bar{\nu} \qquad (2.7)$$
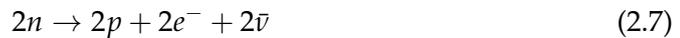
As this decay itself is a process of second order and very rare (half life of $10^{19}$ - $10^{25}$ yr), the choice of the source material for experimental use is crucial. Elements for which a single beta decay is energetically forbidden are particularly suitable. Now if the neutrino fulfills certain requirements then the extremely rare neutrinoless double beta decay $0\nu\beta\beta$ can occur:

$$2n \rightarrow 2p + 2e^- \qquad (2.8)$$

During this process a virtual neutrino is exchanged inside the nucleus. This means that the neutrino would have to be a Majorana particle, that means it would be its own antiparticle. Furthermore the neutrino must have a non-zero mass to enable the helicity flip that is required for this process. The $0\nu\beta\beta$-decay would also violate the lepton number by $\Delta L = 2$, which is forbidden in the Standard Model.

The energy of the $2\nu\beta\beta$-decay is shared between the two electrons and the two neutrinos, leading to a continuous energy spectrum for the sum of the energy of the
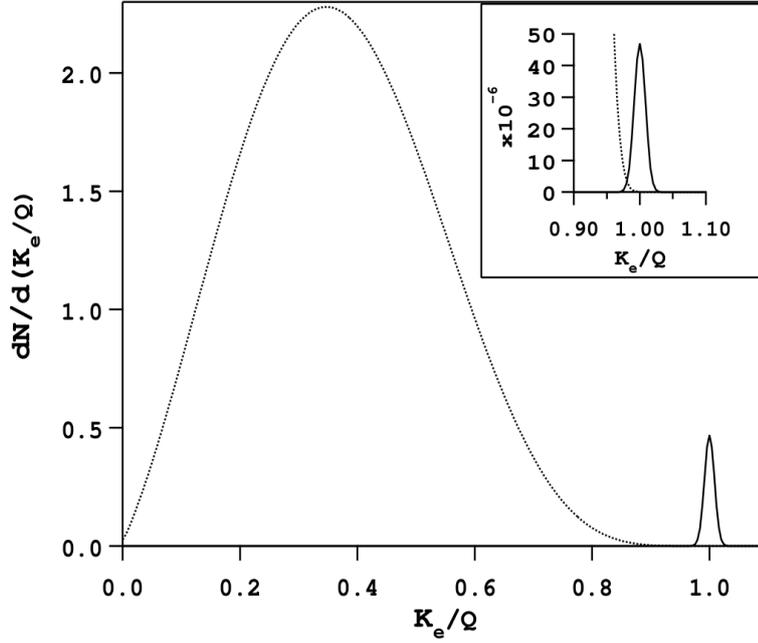
Figure 2.1: Spectrum of the 2νββ-decay (continuous part) and the 0νββ-decay (sharp peak at the maximum energy). $K_e$ is the sum of the two electrons energy and Q is the total energy of the decay. For better visibility the peak is extremely enlarged in this image. Typical rates of about $10^{-5}$ are shown in the inset. (Image taken from [23])

two electrons. On the other hand no neutrinos leave the nucleus at the 0νββ-decay, leading to a sharp peak at the maximum of the continuous spectrum, because the electrons carry away the entire energy of the decay (neglecting the tiny part of energy of the nucleus). The spectrum can be seen in fig. 2.1.

The effective Majorana neutrino mass is accessible through the half life $T_{1/2}$ of the decay.

$$\langle T_{1/2}^{0\nu\beta\beta}\rangle^{-1} \propto \langle m_{\beta\beta}\rangle^2 \tag{2.9}$$

where $m_{\beta\beta}$ is the coherent sum of neutrino mass eigenstates.

$$m_{\beta\beta} = |\sum_i U_{ei}^2 m_i| \tag{2.10}$$

There are several disadvantages of those experiments. First of all, the 0νββ-decay

is model dependent. If the neutrino is a Dirac particle, the $0\nu\beta\beta$-decay does not exist. Moreover the coherent sum includes the Majorana phases $\alpha_i$, which can make the sum very small or even make it vanish. Also the relation between $T^{0\nu\beta\beta}_{1/2}$ and $m_{\beta\beta}$ includes a complicated matrix element which is currently only known to a limited precision.

Among others, the experiments EXO [24], GERDA [25], Majorana [26] and Cuore [27] are trying to investigate the $0\nu\beta\beta$-decay. The currently best limits come from KamLAND-Zen, using $^{136}$Xe and GERDA, using $^{76}$Ge. Depending on the matrix element used for the calculation the effective Majorana neutrino masses upper limit is between $m_{\beta\beta}$ < 61 - 165 meV [28].

### 2.3.3 Neutrino mass limits from single beta decay

The $\beta$-decay has played an important role in neutrino physics ever since considering that inconsistencies in the $\beta$-spectrum led to its postulation and the inverse $\beta$-decay eventually led to its discovery. What makes the single $\beta$-decay so appealing for neutrino mass experiments is the fact that they are completely model independent as they are solely based on kinematics.

The information on the neutrino mass is contained in the endpoint region of the $\beta$-spectrum. Looking at the $\beta$-decay,

$$^{A}_{Z}N \rightarrow\ ^{A}_{Z+1}N' + e^{-} + \bar{\nu}_{e} \tag{2.11}$$

the decay energy is shared between the emitted electron and neutrino. If the neutrino has a mass of zero, then the maximum energy the electron can have is the Endpoint energy $E_0$. In that case the electron gets the entire available energy. However, if the neutrino has a non zero mass then at least the energy it takes to create the neutrino, namely the energy corresponding to its rest mass, must be substracted from $E_0$. This can be seen in fig. 2.2.
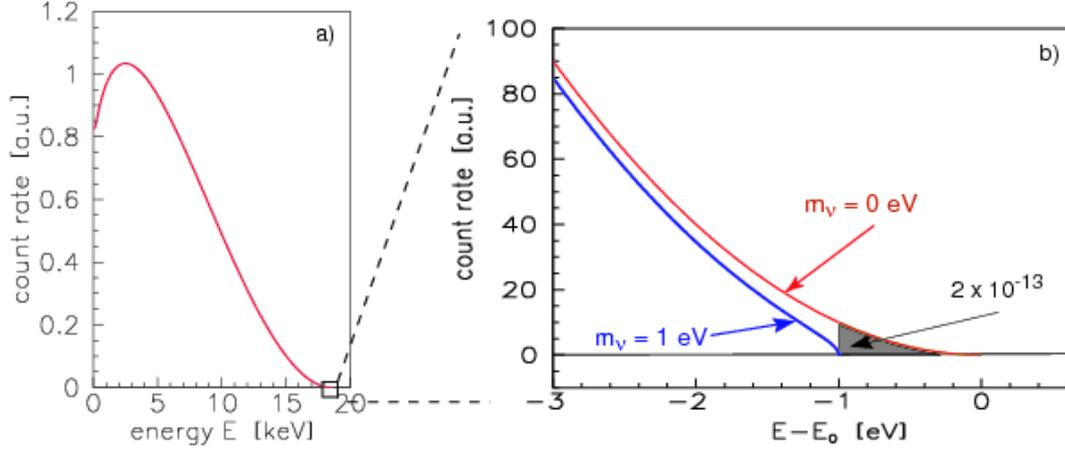
Figure 2.2: Spectrum of the single β-decay for $m_v = 0$ eV (red) and $m_v = 1$ eV (blue). Here it can be seen, that the impact of the neutrino mass is indeed very tiny and most prominent at the endpoint of the spectrum, where in the case of tritium only about $10^{-13}$ of all decay electrons end up. (Image taken from [29])

One of the many difficulties is the requirement of a precise knowledge of the spectrum. The differential spectrum is obtained by the Fermi theory.

$$\frac{\mathrm{d}N}{\mathrm{d}E} = C \cdot F(Z, E) \cdot p \cdot (E + m_e) \cdot (E_0 - E)$$
$$\cdot \sqrt{(E_0 - E)^2 - m_\beta^2} \cdot \Theta(E_0 - E - m_\beta) \tag{2.12}$$

with $F(Z, E)$ being the Fermi function, taking into account Coulomb interactions between daugher nucleus and electron, $p$ being the momentum, $m_e$ the mass and $E$ the kinetic energy of the electron. $E_0$ is the endpoint of the spectrum assuming a neutrino mass of zero $m_\beta = 0$. The constant $C$:

$$C = \frac{G_F^2 \cos(\theta_C) |\mathcal{M}|^2}{2\pi^3} \tag{2.13}$$

contains the Fermi constant $G_F$, the Cabibbo angle $\theta_C$ and the matrix transition element $\mathcal{M}$. One important thing to mention here is that in principle the spectrum is a superposition of three different spectra corresponding to the three different mass eigenstates with the amplitude of each single spectrum corresponding to

11

the squared mixing element $|U_{ei}|^2$ of the respective mass eigenstate to the electron neutrino. With today's state-of-the-art experiments however the energy resolution is not high enough to actually distinguish between the different spectra and so what is measured is the effective electron antineutrino mass $m_\beta$ which is an incoherent sum of the mass eigenstates.

$$m_\beta^2 = \sum_i |U_{ei}|^2 m_i^2 \tag{2.14}$$

Typical elements that are used for single β-decay experiments are Holmium (HOLMES experiment [30] and ECHo experiment [31] via electron capture), Rhenium (Milano experiment [32] and MARE experiment [33]) and Tritium (Project 8 [34] and the KATRIN experiment [8]). In the following the focus will be put on tritium and the KATRIN experiment.

Tritium has a lot of advantages that make it an excellent choice for β-decay experiments. First of all it has one of the lowest endpoints of $E_0 \simeq 18.6$ keV, which is necessary for getting a high enough count rate near the endpoint. For the same reason its low half life of only $T_{1/2} = 12.3$ yr is also advantageous because the need for a huge amount of source material gets mitigated. Furthermore hydrogen is a very well-known element when it comes to theoretical description. Most of it can easily be transferred to tritium $^3$H respectively to the tritium molecule $T_2$. The tritium β-decay is a superallowed decay and the energy independent transition matrix element $|\mathcal{M}|$ is very easy to calculate. At last the low nuclear charge of $Z = 1$ ($^3$H) and $Z = 2$ ($^3$He$^+$) makes calculations generally easier, for example the Fermi function or other quantum mechanical corrections. Also the probability of scattering of the emitted electrons within the source is lower than for nuclei with a higher $Z$.

Unfortunately it is not straightforward to use atomic Tritium. Instead molecular Tritium is utilized.

$$T_2 \rightarrow {}^3HeT^+ + e^- + \bar{\nu}_e \tag{2.15}$$

With tritium in its molecular form however arise new difficulties such as the distribution of its final states. Not only can the daughter molecule be electronically excited, it can also have rotational and vibrational excitations. Those final states have

to be considered in the differential spectrum and equation 2.12 has to be modified in the following way:

$$\frac{\mathrm{d}N}{\mathrm{d}E} = C \cdot F(Z, E) \cdot p \cdot (E + m_e) \cdot \sum_f P_f(E_0 - E - V_f)$$
$$\cdot \sqrt{(E_0 - E - V_f)^2 - m_\beta^2} \cdot \Theta(E_0 - E - V_f - m_\beta) \tag{2.16}$$

with $P_f$ being the probabilities of the final states and $V_f$ the respective energies.

The KATRIN experiment, like its predecessor experiments in Mainz [5] and Troitsk [6], makes use of the MAC-E filter principle, which will be explained in more detail in the next chapter. The currently best direct limit from single β-decay experiments comes from a combined analysis of the Mainz and Troitsk neutrino mass experiments and is given by $m_\beta < 2.0$ eV (95 % C.L.) on the neutrino mass [7].

# Chapter 3

# The KATRIN experiment

The KArlsruhe TRItium Neutrino (KATRIN) experiment aims to reach a sensitivity of 200 meV/c$^2$ (90% C.L.) on the effective electron anti-neutrino mass. For this ambitious goal it is inevitable to make use of state-of-the-art technology as well as an excellent knowledge of the underlying physical model and all the experimental systematic uncertainties. In the following the experimental setup and the measurement principle will be explained. All numbers used in this chapter are just KATRIN design values and may be different to the values actually used during early data taking.

## 3.1 Setup

The whole 70m long experimental setup can be seen in fig. 3.1, startig with the rear section and the Windowless Gaseous Tritium Source (WGTS) over the transport section with Differential Pumping Section (DPS) and Cryogenic Pumping Section (CPS) and the spectrometer section including the Pre Spectrometer (PS) and the Main Spectrometer (MS) and finally ending with the Focal Plane Detector (FPD).

### 3.1.1 Rear section

The main task of the rear section is monitoring and calibration. It controls the electric potential of the source gas and monitors the source gas activity. Later there will also be an angular selective electron gun (E-gun) for monitoring the column density of the source gas by considering scattering at different energies. This E-gun was not yet available for the first data taking phase. Fot that reason it was necessary to look
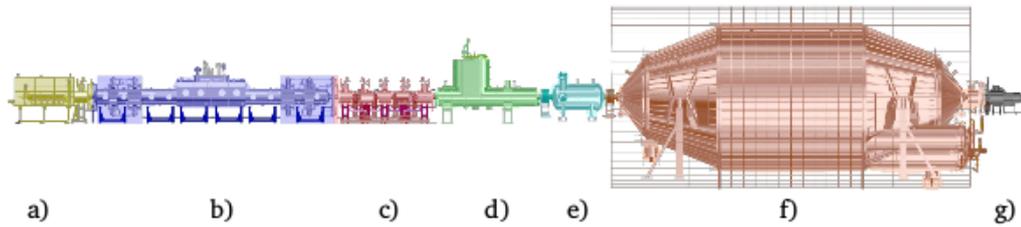
Figure 3.1: All components of the KATRIN experiment setup. a) Rear section, b) Windowless Gaseous Tritium Source WGTS, c) Differential Pumping Section DPS, d) Cryogenic Pumping Section CPS, e) Pre Spectrometer PS, f) Main Spectrometer MS, g) Focal Plane Detector FPD.

for alternative ways to determine the column density. This topic is addressed in chapter 6.

### 3.1.2 Windowless gaseous Tritium source

The source of the KATRIN experiment is a Windowless Gaseous Tritium Source (WGTS). The tube containing the gas is 10 m long and has a diameter of 90 mm. To prevent energy loss due to scattering on any solid material the source was designed to be windowless. This in turn calls for pumping of the outgoing gas on both sides of the source tube. The pumped gas is fed back into the source through the inner loop system in order to obtain constant conditions inside the source regarding density and gas composition. The column density is kept at a constant level of $\rho d = 5 \cdot 10^{17}$ cm$^{-2}$. This number is a trade-off between high luminosity and reduced scattering probability of the emitted electrons with the remaining source gas. It corresponds to about $10^{11}$ decays per second with isotropical angular distribution. Furhermore the gas is constantly cooled to a stable temperature of 30 K to keep energy smearing by the thermal Doppler effect to a minimum. The gas itself has a very high purity of 95% $T_2$ and only small amounts of other isotopologues DT and HT as well as tiny amounts of $D_2$ or $H_2$. The whole WGTS is set on a magnetic field of 3.6 T which causes the electrons emitted in forward direction to move with a cyclotron motion around the magnetic field lines in the direction of the spectrometer section. Altogether the source is constructed in a way to ensure maximal luminosity with minimal systematic effects. Keeping the source gas at a very high stability is

also one key property since even small fluctuations have huge impact on the signal that KATRIN is looking for.

### 3.1.3 Differential pumping section

The purpose of the transport section is the reduction of residual gas coming from the windowless source by a factor of $10^{14}$ to prevent any gas entering the spectrometer section and the adiabatic guidance of electrons to the spectrometer. The adiabatic guidance is part of the MAC-E filter principle, which will be explained later. The first part of the transport section is the differential pumping section (DPS). The DPS consists of 5 parts that are tilted with respect to each other by 20°. While the electrons are guided through the DPS via magnetic fields, the neutral gas molecules collide with the walls and are eventually pumped out by one of the four Turbomolecular Pumps (TMP) sitting between the beamtube elements. Positive ions are in principle also following the magnetic field lines just like the electrons, but they are trapped inside the DPS from both sides. On the source side they get repelled by the gas pressure while a slightly more positive potential on the other side stops them from escaping the DPS. In the end the ions are removed by the $\vec{E} \times \vec{B}$-drift of an electric dipole. The DPS reduces the tritium flow by a factor of $10^7$.

### 3.1.4 Cryogenic pumping section

The cryogenic pumping section (CPS) has the task to remove any residual traces of gas that made it through the DPS. Its tube elements, which are also tilted by 20°, are cooled down to a temperature of just a few Kelvin above absolute zero. They are covered with Argon frost that passively adsorbs the remaining gas molecules when they hit the walls of the CPS. The CPS reduces the tritium flow by another factor of $10^7$ so that after the whole transport section a reduction factor of $10^{14}$ is achieved.

### 3.1.5 Pre spectrometer

Before the electrons coming from the transport section can enter the main spectrometer they first have to pass the pre spectrometer. The pre spectrometer is set on a retarding potential of 18.3 keV, reflecting all electrons that have less energy than at least 300 eV below the maximally reachable endpoint energy $E_0$. The first reason

for this is that electrons can ionize rest gas in the main spectrometer which leads to unwanted background. The second reason is that a high electron density in the front part of the main spectrometer can influence the retarding potential and thus disturb the high-precision β-spectroscopy of the endpoint region. After the pre spectrometer only about $10^3$ electrons per second enter the main spectrometer. Both the pre and the main spectrometer work with the Magnetic-Adiabatic-Collimation combined with an Electrostatic (MAC-E) filter principle, which will be explained in more detail in section 3.2.

### 3.1.6 Main spectrometer

In the main spectrometer the electrons get analyzed by an ultra stable retarding potential that scans a range around the endpoint region of the spectrum in order to perform an integral measurement. The whole vessel has a length of almost 24 m and a diameter of 10 m. The size is necessary to ensure the electrons adiabatic motion and to prevent the signal electrons from hitting the walls as the magnetic flux tube widens with the decreasing magnetic field inside the main spectrometer. The magnetic field has to be decreased by four orders of magnitude within the spectrometer following the MAC-E filter principle which will be introduced in section 3.2. By using this measurement principle the KATRIN spectrometer reaches an excellent energy resolution of $\Delta E = 0.93$ eV at an electron energy of 18.6 keV. To counter background coming from electrons interacting with gas molecules the spectrometer is connected to a vacuum system providing a pressure in the range of only $10^{-11}$ mbar. This ultra high vacuum is the same as on the moon's surface. Further background can occur in the form of electrons from the vessel walls. Those electrons get reflected by the inner electrode system. This system consists of thin wires placed in a short distance to the spectrometer walls that also allow for fine tuning of the electric field inside the spectrometer. The huge aircoil system around the main spectrometer vessel compensates for the earth magnetic field.

### 3.1.7 Focal plane detector

The electrons that make it through the voltage barrier of the main spectrometer will be re-accelerated and eventually be counted by the focal plane detector (FPD). The re-acceleration helps to discriminate the signal electrons from background. Only

Figure 3.2: The FPD and its 148 pixels. The bullseye has 4 pixels and the 12 rings have 12 pixels each. Every pixel has the same area. [35]

about one electron per second will hit the silicon detector that has a diameter of 90 mm. The detector is divided into 148 pixels of equal area to provide good spatial resolution. Fig. 3.2 shows the detector layout.

The segmentation into pixels allows for a precise mapping of inhomogenities in the retarding potential and magnetic fields of the experimental setup by measuring an independent β-spectrum in each pixel.

Due to the very low count rate per pixel in the signal region there is need for an extremely low background. Therefore the detector system has active and passive shieldings against cosmic background. Moreover the energy resolution of about 1 keV is used for further background discrimination. Although there is a very low count rate per pixel in the signal region, the detector is also able to handle higher rates for calibration measurements.

## 3.2 Measurement principle of the MAC-E Filter

The electrons are emitted isotropically in the WGTS. Electrons that are emitted in forward direction will be guided in the direction of the spectrometers by magnetic fields. However, the electrons that are not emitted with an angle of $\theta = 0°$ to the magnetic field lines will be forced on a cyclotron motion around the magnetic field
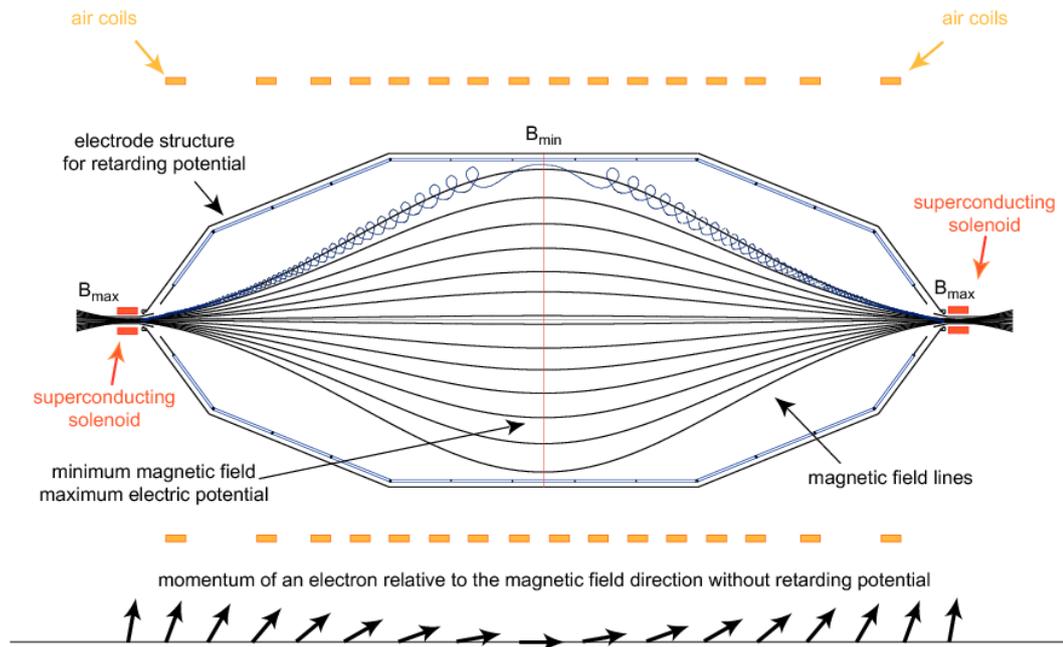
Figure 3.3: The MAC-E Filter principle. By reducing the magnetic field by four orders of magnitude, the transversal part of the electrons energy gets transformed into parallel energy. The maximal transversal energy that electrons still can have at the analyzing plane determines the energy resolution of the spectrometer. (Image taken from [36])

lines. This means that the electrons energy can be split into a parallel and transversal part with respect to the magnetic field lines.

$$E_{kin} = E_{\parallel} + E_{\perp} \tag{3.1}$$

The spectrometer works as a high-pass filter. Only the electrons that have a higher energy than the retarding potential can pass. In the analyzing plane however only the parallel part $E_{\parallel}$ is analyzed by the electrostatic filter. Consequently the transversal part $E_{\perp}$ needs to be transformed into $E_{\parallel}$ to achieve both high count rates and a good energy resolution. This can be realized by making use of the MAC-E filter principle, which can be explained with fig. 3.3.

The magnetic field has to be reduced by four orders of magnitude from the

entrance of the spectrometer to the analyzing plane. This has to happen adiabatically to ensure that the magnetic moment $\mu$ is conserved, hence the big size of the spectrometer.

$$\frac{E_\perp}{B} = \mu = \text{const.} \tag{3.2}$$

From equation 3.2 it can be seen that by reducing the magnetic field, the transversal energy $E_\perp$ gets reduced simultaneously. This can only be done to some extent, since the magnetic flux (eq. 3.3) is constant at all times.

$$\Phi = \int_A \vec{B} \, d\vec{A} = \text{const.} = 191 \, \text{Tcm}^2 \tag{3.3}$$

Consequently, lowering the magnetic fields increases the size of the flux tube. That size is limited by the diameter of the spectrometer vessel. As a result of this, there is a maximal transversal energy, that can not be transformed. This energy determines the energy resolution of the spectrometer by:

$$\Delta E = \frac{B_{min}}{B_{max}} \cdot E \tag{3.4}$$

For electrons with an energy close to the endpoint the resolution is $\Delta E = 0.93$ eV. As can be seen in fig. 3.3, after the analyzing plane the magnetic field increases again up to the maximal magnetic field $B_{max}$ at the pinch magnet between main spectrometer and the detector. The same maximal magnetic field is applied at the entrance of the main spectrometer. When the magnetic field becomes higher than in the source it causes the transversal energy to increase above its initial value. The moment the angle exceeds 90°, the electrons are reflected by the magnets and return to the source. This is known as a magnetic mirror. Since the magnetic field at the pinch magnet is higher than the one in the source, where the electrons are emitted, not all electrons emitted in forward direction can reach the detector, even if they had enough energy to overcome the retarding potential in the main spectrometer. The point in doing this is that electrons with a larger starting angle will perform the cyclotron motion with a bigger radius, effectively lengthening the electron's path through the source. This in turn increases the probability of the electron being scattered and the amount of energy loss via synchrotron radiation.

Theoretical Beta Spectrum    x    Response function   →   Integrated Spectrum
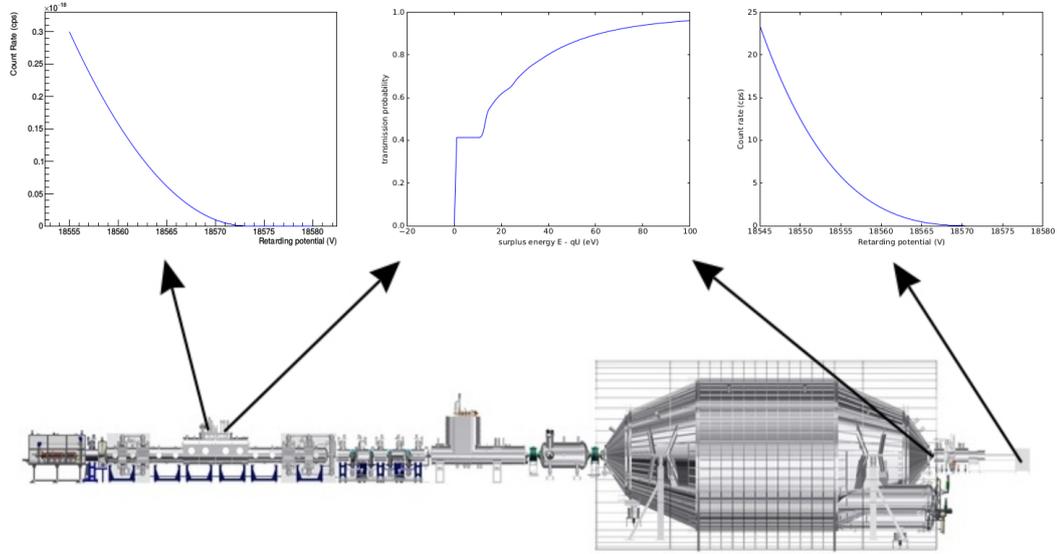


Figure 3.4: The differential spectrum of the electrons emitted in the source gets convoluted with the experimental response function to create the integrated spectrum

The magnetic fields are set in a way to only allow electrons up to a maximal starting angle $\theta_{max} \simeq 51°$ to be measured.

$$\theta_{max} = \arcsin\left(\sqrt{\frac{B_S}{B_{max}}}\right) = \arcsin\left(\sqrt{\frac{3.6\text{T}}{6\text{T}}}\right) = 50.77° \tag{3.5}$$

With $B_S$ being the magnetic field in the source. All electrons that are emitted under $\theta > \theta_{max}$ get reflected by $B_{max}$.

## 3.3 Modeling of the Spectrum

The underlying model that is used to simulate the measured spectrum can be split in three parts, as illustrated in fig. 3.4.

The first part is the differential beta decay spectrum as introduced in chapter 2.3 (eq. 2.16). The second part is the response function of the experiment which
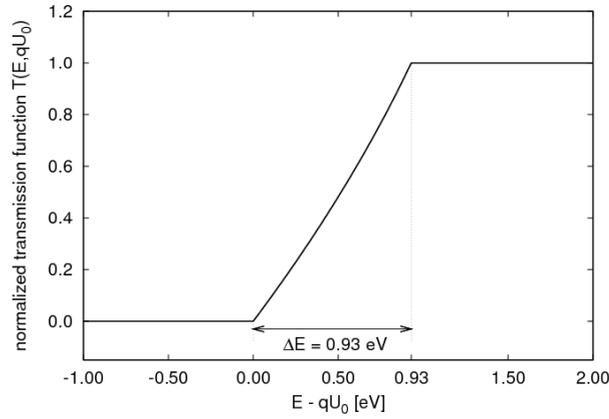
Figure 3.5: The transmission function is a transmission probability for electrons of a certain energy to overcome the retarding potential in the analyzing plane. (Slightly changed image from [37])

describes effects of the source and the spectrometer. The spectrometer properties are represented by the transmission function (normalized):

$$
T(E, qU) = \begin{cases} 0 & E - qU \leq 0 \\ \dfrac{1 - \sqrt{1 - \frac{E-qU}{E}\frac{B_S}{B_A}\frac{2}{\gamma+1}}}{1 - \sqrt{1 - \frac{B_S}{B_{max}}}} & 0 \leq E - qU \leq \Delta E \\ 1 & E - qU > \Delta E \end{cases} \tag{3.6}
$$

With $B_S$ being the source magnetic field and $B_A$ being the magnetic field of the analyzing plane. It is the transmission probability for electrons of a certain surplus energy $E - qU$ and any starting angle related to $B_S/B_A$ for a given retarding potential $qU$. The transmission function is illustrated in fig. 3.5.

As already mentioned in the section about the MAC-E Filter, electrons are emitted isotropically in the source. Electrons that are emitted under a starting angle of $\theta = 0°$ need at least the energy that is set by the retarding potential to be able to pass the analyzing plane. Electrons with a starting angle $\theta > 0°$ will have a finite amount of transversal energy that is not seen by the analyzing plane. Those electrons need some surplus energy to be able to overcome the potential which
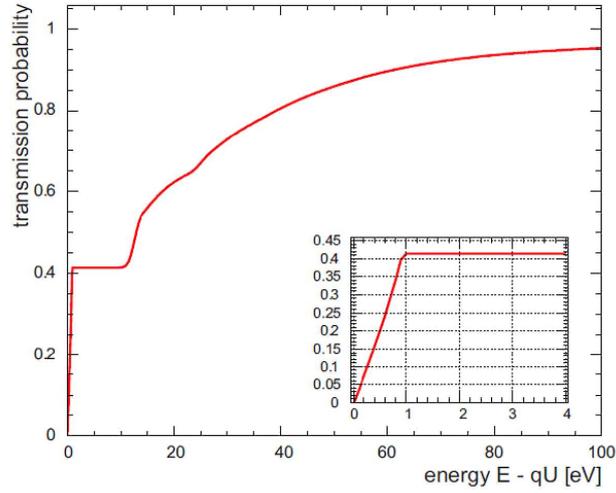
Figure 3.6: The response function of the KATRIN experiment. About 41% of electrons leave the source unscattered. As those electrons have not suffered energy loss through scattering they just follow the transmission function shown in the inset. The mean energy loss of inelastic scattering is about 13 eV. That is where the response function has its second step that corresponds to electrons that have scattered once before leaving the source. (Image taken from [38])

peaks at $\Delta E = 0.93$ eV for electrons that are emitted under the maximal starting angle $\theta_{max}$.

The Response function is a convolution of spectrometer properties, namely the transmission function $T(E, qU)$ and source properties like scattering.

$$R(E, qU) = \int\limits_{\epsilon=0}^{E-qU} T(E - \epsilon, qU) \cdot (P_0\delta(\epsilon) + P_1 f(\epsilon) + P_2(f \otimes f)(\epsilon) + ...) \, d\epsilon \quad (3.7)$$

Here the $P_i$ are the scattering probabilities for i'th scattering and $f(\epsilon)$ is the energy loss function, describing the probability of loosing a certain amount of energy $\epsilon$ during a scattering. This leads to an actual transmission probability as a function of starting energy. The response function is shown in fig. 3.6.

At last the third part in fig. 3.4 shows the integrated spectrum which is eventually
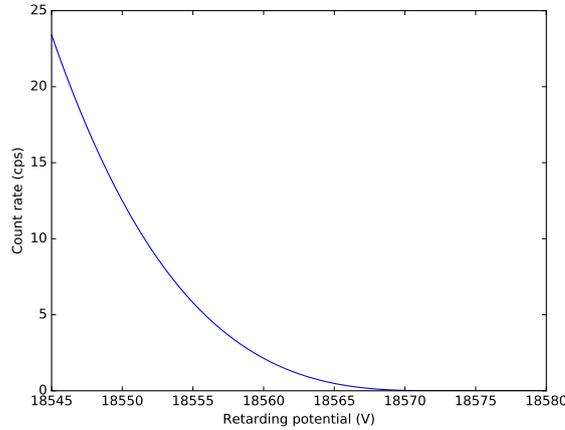
Figure 3.7: The integrated spectrum is a convolution of the differential spectrum and the response function.

measured by the detector. It is a convolution of the differential spectrum (eq. 2.16) and the response function (eq. 3.7).

$$\mathrm{d}\dot{N}(qU) = N \cdot \int\limits_{qU}^{E_0} \frac{\mathrm{d}\Gamma}{\mathrm{d}E}(E_0, m_\nu^2) \cdot R(E, qU) \, \mathrm{d}E \tag{3.8}$$

where $N$ is a normalization that consists of the maximal starting angle of electrons $\theta_{max}$, the tritium purity in the source $N_T$ and the efficiency $\epsilon$ of the detector. A simulated integral spectrum can be seen in fig. 3.7.

At last the model has to take into account pixel dependent effects. Those effects include inhomogenities in the retarding potential and the magnetic fields as well as gas properties in the source such as temperature, density and velocity asymmetries. Also the background is different for all pixels. Consequently every pixel can be modeled with its own differential spectrum and response function. Fig. 3.8 shows an example what a pixel dependent magnetic field can look like.
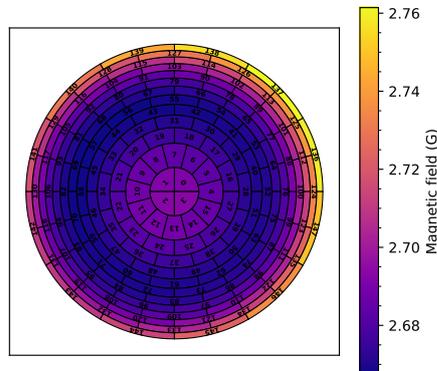
Figure 3.8: Example of a pixel dependent magnetic field.

## 3.4  Analysis Software tools

The KATRIN collaboration has very sophisticated and advanced software tools to model and fit the data available.

### 3.4.1  SSC and KaFit

The official software of the KATRIN collaboration is the Source and Spectrum Calculation (SSC) written in C++ [39][40]. It is based on the previously described model in chapter 3.3, which is just a basic description with no mention of any corrections or details. SSC includes all known theoretical and experimental effects in detail. The effects can be turned on and off individually which makes it possible to examine their influence on the spectrum and the fitting parameters one by one as explained in further detail in the next chapter. SSC provides the theoretical spectrum normalized to one second. In order to actually simulate data the measuring time distribution (MTD) is needed. The MTD contains the retarding potentials at which the measurement takes place and the time intervals spent at each potential. The theoretical spectrum gets combined with the MTD by the attending framework KaFit, which can also perform a poissonian randomization of the simulated rates. While SSC provides the theoretical spectrum, KaFit is used as a fitting tool. KaFit can read in data and minimizes a negative log-likelihood with respect to the four

parameters endpoint $E_0$, neutrino mass squared $m_\nu^2$, signal rate $R_{Sig}$ and background rate $R_{Bg}$ as highlighted in equation 3.9:

$$\mathrm{d}\dot{N}(qU) = R_{Sig} \cdot \int\limits_{qU}^{E_0} \frac{\mathrm{d}\Gamma}{\mathrm{d}E}(E_0, m_\nu^2) \cdot R(E, qU)\ \mathrm{d}E + R_{Bg} \tag{3.9}$$

The likelihood is minimized by the classical minimizer Minuit but KaFit can also perform a Bayesian analysis by using Monte Carlo Markov Chains. SSC and KaFit are under constant improvement and optimization by the collaboration. Within the frame of this thesis SSC and KaFit were mainly used for sensitivity studies and the study of systematic effects as elucidated in the next chapter.

### 3.4.2 Fitrium

Fitrium [41] is a new C++ code describing the integrated spectrum of the KATRIN experiment. It is designed to work fast and can handle many free parameters. For this purpose it uses caching mechanisms and is parallelizable. In Fitrium it is possible to treat control parameters such as the different magnetic fields or the column density as fit parameters and to apply pull terms to the likelihood for all fit parameters. It is also possible to switch from a poissonian to a gaussian likelihood in order to treat systematic effects by using covariance matrices describing the uncertainties of control parameters. Besides systematic effects like the doppler effect, Fitrium also includes energy dependent effects like an energy dependent inelastic cross section and an energy dependent detector efficiency which were implemented in the frame of this thesis. Within the frame of this thesis Fitrium was used for accuracy studies shown in the next chapter, for the analysis of the First Tritium data shown in chapter 5 and the column density determination in chapter 6.

# Chapter 4

# Sensitivity studies

After a short overview of how the sensitivity is calculated this chapter contains a table of some selected systematic effects and their impact on the neutrino mass fit results as well as a short explanation of how the size of those effects can be obtained. The main purpose of this chapter is to investigate the importance of effects at different stages of the KATRIN experiment. As measurement time passes the statistical uncertainty gets smaller and consequently the treatment of systematic effects gets more important. In the conclusion of this chapter the results are summarized.

The sensitivity on the neutrino mass in the KATRIN experiment is defined in the following way. Assuming a gaussian distribution of the estimates of $m_\nu^2$ the sensitivity is determined by the total uncertainty $\sigma_{total}$:

$$S_{m_\nu}(90\% \text{ C.L.}) = \sqrt{1.645 \cdot \sigma_{total}} \qquad (4.1)$$

with the total error composed of statistical and systematic uncertainties:

$$\sigma_{total} = \sqrt{\sigma_{stat}^2 + \sigma_{syst}^2} \qquad (4.2)$$

The statistical uncertainty $\sigma_{stat}$ decreases with measurement time. The size of the statistical uncertainty depends on the measuring time distribution (MTD), especially regarding the size of the measurement interval, and of the background rate of the experiment. The statistical uncertainty gets better with an increasing measurement interval and worse with an increasing background rate. The sensitivity of the KATRIN experiment as a function of total measuring time is limited by the value of the systematic uncertainty. Using the values of the KATRIN design report the statistical

uncertainty gets small enough to approach the value of the systematic uncertainty asymptotically after three years of measuring time, leading to the final sensitivity. With the originally assumed values of the MTD and a background of 10 mcps the statistial uncertainty after three years was determined to be $\sigma_{stat} = 0.0166$ eV$^2$ [39]. Even though the quadratic sum of all known systematic errors is smaller than this, the systematic budget is chosen to be in the same order as the statistical error so that unidentified effects can be included, giving $\sigma_{syst} = 0.017$ eV$^2$. Plugging those numbers in equations 4.2 and 4.1 gives a sensitivity of $S_{m_\nu}$(90% C.L.) = 198 meV. This number can be interpreted as an upper limit on the neutrino mass in case KATRIN does not find the neutrino mass. At the same time a neutrino mass of $m_\nu$ = 350 meV can be measured at a level of $5\sigma$.

## 4.1 Table of Systematics

The systematic shift of the neutrino mass induced by neglecting a single effect can be obtained in the following way. Two spectra need to be created, one of them including an effect and the other one neglecting it. Otherwise both spectra need to be identical. The neutrino mass is set to zero in both spectra. The spectrum including the effect is combined with a MTD to generate some data without statistical fluctuations. The generated data get fitted to the spectrum neglecting the effect. If the effect in question has influence on the shape of the spectrum in a way that it can mimic or shift a neutrino mass signal, then a fit based on a model neglecting that effect should return a certain non-zero value for the squared neutrino mass even though it was set to zero in the generated data. The size of the result determines the systematic shift of the squared neutrino mass produced by this effect. Note that this procedure just states the shift of the squared neutrino mass if the effect is completely neglected and does not make any statement on the uncertainty by an imprecise knowledge of the effect.

In the end all systematic uncertainties get added quadratically to give the total systematic uncertainty $\sigma_{syst}$. This holds only if the systematic effects are uncorrelated. Table 4.1 contains an overview over some of the most important systematic effects and their corresponding shifts of the squared neutrino mass. The systematic effects

included in table 4.1 are [40]:

- **Doppler effect:** There are two sources of the doppler effect. The first doppler effect comes from the bulk velocity of the gas flow. The gas is pumped into the WGTS at the middle of the tube and flows to both ends, where it is pumped out. The doppler effect coming from this motion of the gas is tiny as the velocity of the gas is very small. The second and more important doppler effect comes from the thermal motion of the gas molecules. Even though the source gas is cooled down to a temperature of only 30 K, the tritium molecules still have enough energy to produce a considerable doppler effect. In SSC this effect can be incorporated in two different ways. In the first way the doppler effect is included in the final states distribution (FSD) by a broadening of the distribution. This way only the thermal effect can be included. If the doppler effect coming from the bulk velocity also needs to be included there is also the way to directly incorporate both doppler effects (thermal and bulk) in the calculation of the integrated rate by convoluting the differential spectrum with a broadening kernel. Both ways are represented in table 4.1 and produce nearly the same shift of the squared neutrino mass if neglected.

- **Relativistic corrections on Transmission function:** The transmission function contains the relativistic gamma factor $\gamma$ as can be seen in the equation for the transmission function (eq. 3.6). Neglecting this factor leads to a shift of the squared neutrino mass.

- **Detailed magnetic field inside WGTS:** The magnetic field inside the WGTS is not completely constant. There is a magnetic field profile along the z axis of the source. Small deviations of the magnetic field at the pump ports are present that induce a small shift of the squared neutrino mass if neglected.

- **WGTS Segmentation:** SSC can divide the WGTS into slices in order to properly take effects with a z-dependence into account. Dividing the WGTS into slices for generating data, but setting only one slice in the model that is used for fitting does not produce any noticable shift on the fit parameters by its own. Only after z-dependent effects like the detailed magnetic field are active

in both spectra (generated data spectrum and model spectrum) a shift of the squared neutrino mass can be seen.

- **Detailed Transmission function for zero Scatterings:** Electrons are emitted isotropically in the source. For the standard transmission function the assumption is made that the distribution of electrons between a starting angle of $\theta = 0°$ and $\theta_{max}$ is isotropic. In reality electrons with smaller starting angles have a higher chance of leaving the source without scattering while electrons with higher starting angles are more likely to scatter off gas molecules because of their longer path inside the source gas. After scattering some of the electrons do not have enough energy to overcome the retarding potential anymore. Consequently the angular distribution of electrons leaving the source is not isotropic anymore. There is an angular distribution of electrons having undergone a specific number $i$ of scatterings and a corresponding transmission function $T_i^*(E, qU)$ for every number of scatterings. The detailed transmission function for zero scatterings $T_0^*(E, qU)$ has by far the biggest influence. $T_0^*(E, qU)$ is used in the generated data. Higher numbers of scatterings are calculated with the standard transmission function. Neglecting this effect and fitting only with the standard transmission function leads to the shift of the squared neutrino mass shown in table 4.1.

- **1D Gasdynamics:** The source gas dynamics can be modeled including temperature, velocity and density asymmetries. Neglecting these and instead using constant averaged values of those parameters for fitting leads to a systematic shift of the squared neutrino mass.

- **Radiative corrections:** The radiative correction factor describes electromagnetic effects including virtual and real photons. Of all theoretical corrections this effect produces the highest shift of the squared neutrino mass if neglected.

- **Energyloss due to Synchrotron radiation:** Electrons with a starting angle $\theta > 0°$ will perform a cylotron motion around the magnetic field lines and thereby lose energy via synchrotron radiation. The higher the starting angle, the more energy is lost via this effect. Electrons with a starting angle of zero do not emit synchrotron radiation. The neglect of this effect produces the highest shift of the squared neutrino mass of all effects listed in table 4.1.

Table 4.1: Table of systematic effects and their corresponding shift on the squared neutrino mass [40].

| Effect | Description | Shift of $\Delta m_\nu^2$ in $10^{-3}$ eV$^2$ |
|---|---|---|
| Doppler effect | broadening FSD | -18 |
| Doppler effect | calculated in integral (thermal and bulk) | -17.4 |
| Relativistic corrections on Transmission function | | -5.6 |
| Detailed magnetic field inside WGTS | mag. field profile along z axis | 1.9 |
| WGTS 1 Slice for analysis | (100 Slices in Simulation) | 0.005 |
| WGTS 1 Slice for analysis | (100 in Sim., both with detailed magnetic field) | -4.5 |
| Detailed Transmission function for zero Scatterings | taking non-isotropic dist. of $e^-$ after scattering into account | 12.1 |
| 1D Gasdynamics | including Temperature, velocity and density asymmetry | -3.8 |
| Radiative corrections | | -1.97 |
| Energyloss due to Synchrotron radiation | | -31.4 |

## 4.2 Analysis model at different stages of the KATRIN experiment

For data being analyzed at earlier times than the full three years, there are different constraints on the analysis model. Usually the systematic uncertainty is chosen to be on the same level as the statistical uncertainty and therefore the model can be adjusted to fit the required level of uncertainty for different times.

$$\sigma_{stat} \overset{!}{=} \sigma_{syst} \tag{4.3}$$

This allows neglecting certain computationally expensive effects in an early analysis and leads to more loose boundaries on the accuracy of some parameters.

As mentioned above, the statistical uncertainties are strongly dependent on the measuring time distribution and the background. In order to predict a value of the uncertainty for different times during the measurement phase, the settings chosen for the simulation have to correspond as close as possible to the real settings.

At this point it is very important to make it clear that the statistical uncertainty is different to the originally calculated value of $\sigma_{stat} = 0.0166$ eV$^2$ after three years. The main reason for this is the fact that during background measurements the background rate turned out to be higher than expected. This caused a significant increase of the statistical uncertainty and thereby a worsening of the sensitivity. To counter this the magnetic field settings were slightly changed. The magnetic field at the analyzing plane was chosen to be larger than the original value of $B_A = 3\cdot10^{-4}$ T = 3 G. This way the magnetic flux tube radius was decreased. As a consequence a lower number of background electrons originating from inside the spectrometer could reach the detector. On the other hand the resolution of the spectrometer was worsened as can be seen in equation 3.4. Simulations where both effects were balanced against each other revealed that the best sensitivity can be achieved by setting the magnetic field $B_A$ = 9 G [42]. For technical reasons all magnetic fields of the entire setup were lowered by 30% leading to the values of the magnetic fields that are shown in the tables 4.2 and 4.3. An additional point is the fact that the MTD has a significant influence on the statistical uncertainty as well. For the studies that are presented in this chapter a flat time distribution with a range of 60 eV below the endpoint was used (see table A.2).

The evolution of the statistical uncertainty as a function of measuring time can be seen in fig. 4.1 while the evolution of the sensitivity as a function of time is shown in fig. 4.2, setting $\sigma_{stat} = \sigma_{syst}$ at all times.

In the following the measurement will be divided into three sections: the low statistics measurement, the time after which the sensitivity on the neutrino mass reaches 1eV and the full three years measurement. For each of those areas the settings can slightly differ, depending on the anterior results and information gained during earlier measurements.
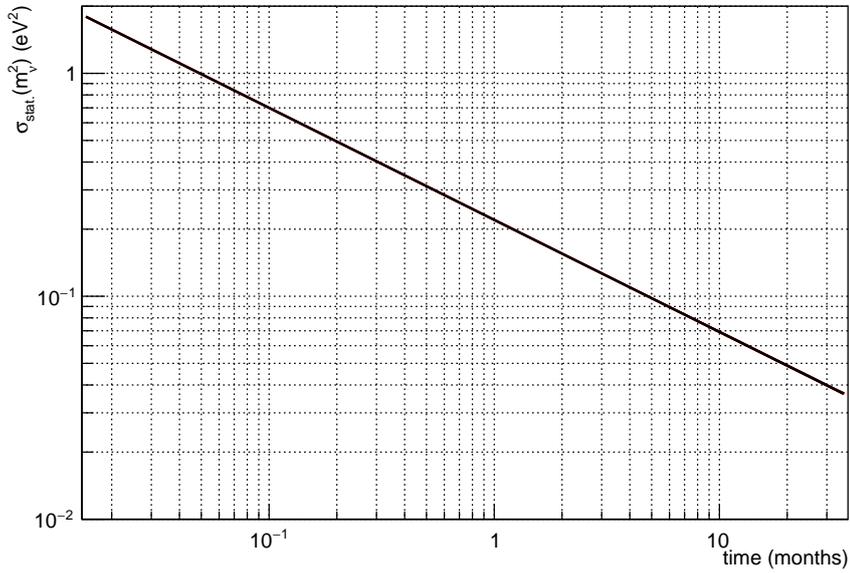
Figure 4.1: The statistical uncertainty $\sigma_{stat}$ as a function of measuring time assuming a magnetic field of 9 G at the analyzing plane and a background rate of 225 mcps.
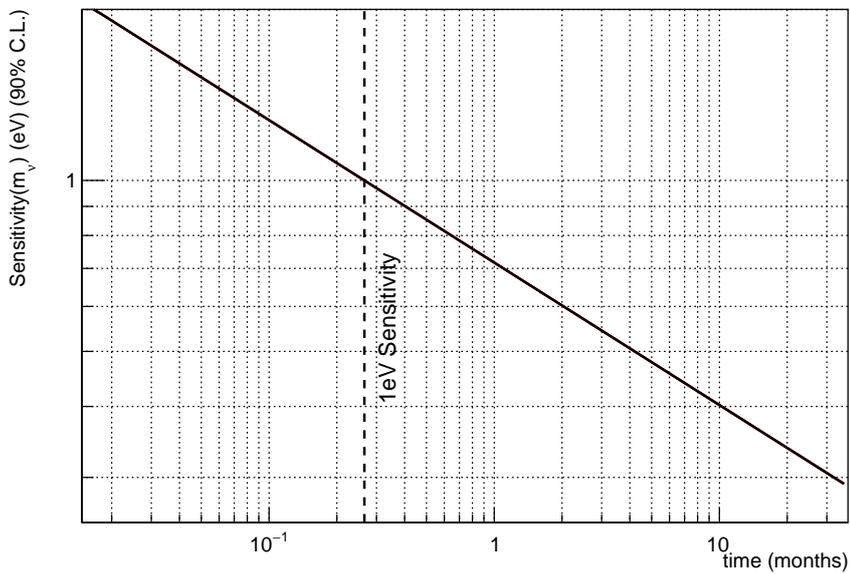


Figure 4.2: Sensitivity as a function of time, assuming $\sigma_{stat} = \sigma_{syst}$ at all times.

Table 4.2: Settings used for beforehand simulations of the low statistics measurement.

| Parameter | Value |
|---|---|
| Column density | $2.5 \cdot 10^{21} \dfrac{1}{m^2}$ |
| $B_{Source}$ | 2.52 T |
| $B_{max}$ | 4.2 T |
| $B_{ana}$ | $6 \cdot 10^{-4}$ T |
| Bg | 225 mcps |
| Tritium purity | 0.01 |
| WGTS Temperature | 30 K |

### 4.2.1 Low statistics measurement

The simulations of this segment were performed before the First Tritium campaign but were inspired by it. Table 4.2 shows the settings that were assumed for the simulations. The MTD used for the simulations can be found in table A.1 in the appendix.

With a total measuring time of 7 days KaFit calculates the statistical uncertainty to be $\sigma_{stat} = 10.41$ eV$^2$. That means, setting the systematic uncertainty to the same value and using equations 4.1 and 4.2, the sensitivity on the neutrino mass is $S_{m_\nu}(90\%$ C.L.) = 4.921 eV.

### 4.2.2 Sensitivity of 1eV

Once the main measurement phase starts, the source will have its full activity. For the estimation of the statistical uncertainty a flat time distribution is assumed covering the range [$E_0$ - 60 eV, $E_0$ + 5.0 eV]. The settings and time distributions for the simulations are shown in the tables 4.3 (settings) and A.2 (MTD).

For those settings the statistical uncertainty reaches the value $\sigma_{stat}$ = 0.4299 eV$^2$ after about 0.265 months ($\simeq$ 8.08 days) runtime, which corresponds to a sensitivity of $S_{m_\nu}(90$ % C.L.) = 1 eV (setting $\sigma_{stat} = \sigma_{syst}$).

Table 4.3: Settings used for simulations of the full measurement phase

| Parameter | Value |
|---|---|
| Column density | $5 \cdot 10^{21} \frac{1}{m^2}$ |
| $B_{Source}$ | 2.52 T |
| $B_{max}$ | 4.2 T |
| $B_{ana}$ | $6 \cdot 10^{-4}$ T |
| Bg | 250 mcps |
| Tritium purity | 0.95 |
| WGTS Temperature | 30 K |

### 4.2.3 Full measuring time

The KATRIN experiment will run for five calendar years including offline time for maintenance. The full run-time will be three years. For simulations the same settings as in section 4.2.2 are assumed. Here KaFit gives a statistical uncertainty of $\sigma_{stat} = 0.0368$ eV$^2$ after three years. As a short reminder, this value differs from the originally calculated value of $\sigma_{stat} = 0.0166$ eV$^2$ because the magnetic fields are different to the originally planned ones as explained above.

In fig. 4.2 it can be seen that after three years of measurement a sensitivity of $S_{m_\nu}$(90% C.L.) = 293 meV can be achieved (setting $\sigma_{stat} = \sigma_{syst}$). Holding onto the original systematic budget of $\sigma_{syst} = 0.017$ eV$^2$ the sensitivity can be enhanced to a value of $S_{m_\nu}$(90% C.L.) = 258 meV. Further improvement of the sensitivity can be reached by optimizing the MTD. For the studies in this chapter a simple flat time distribution was chosen.

## 4.3 Evaluation

Eventually the size of the systematic effects is compared to the statistical uncertainty at the different stages to justify a possible neglect of computationally expensive effects in the analysis. Table 4.4 is showing the size of the three systematic effects of table 4.1 with the biggest shifts relative to the size of the statistical uncertainty at different stages of the experiment. Those effects are the doppler effect, the synchrotron radiation and the transmission function for non-isotropic angular distribution

of electrons. The portions shown in table 4.4 come from a direct comparison of the shift of a single effect and the statistical uncertainty at the three stages. For getting the total systematic uncertainty those values need to be added in quadrature:

$$\sigma^2_{syst.,total} = \sigma^2_{syst.1} + \sigma^2_{syst.2} + \sigma^2_{syst.3} + ... \tag{4.4}$$

That means that for getting the portion of one of the systematic effects compared to the systematic budget the values in table 4.4 need to be squared. Corresponding to this fig. 4.3 shows the time at which the different individual effects reach 10% of the statistical uncertainty. From this it can be seen that neither for the low statistics measurement nor for the time at which the sensitivity reaches 1 eV during the full measurement any of the systematics of table 4.1 gets bigger than 10 % of the statistical uncertainty. Especially for the low statistics data all effects individually have very small impact due to the high statistical uncertainty and can in principle be neglected regarding a neutrino mass measurement. Because of the low sensitivity on the neutrino mass however it will not be considered as a fit parameter during the First Tritium campaign.

Table 4.5 shows the necessary accuracy on some of the parameters to not contribute more than 10% to the systematic budget: $\Delta m_\nu^2 \overset{!}{\leq} 0.1\,\sigma_{stat}$. This was done by varying the value of a parameter in small steps in the generated data spectra. Then those spectra were fitted with a fixed value of the parameter in question. That way the systematic shift can be plotted as a function of relative offset of a parameter. Fig. 4.4 shows this plot exemplary for the column density. If the model spectrum that is used for fitting data takes a wrong value for the column density, deviating by x% from the true value, the squared neutrino mass will be shifted by y(x) eV$^2$.

The values of the precision requirements after 3 years of measurement in table 4.5 are remarkably small. Especially the required 0.016% precision on the column density can very likely not be reached. The KATRIN design report states an uncertainty of 0.1% on the column density. That is one order of magnitude bigger than the 0.016% that are needed. With an uncertainty of 0.1% on the column density the neutrino mass shift would take up about $\Delta m_\nu^2 = 0.022$ eV$^2$ which is about 60% of the systematic budget. This is caused by the choice of the measuring time distribution. The size of systematic shifts is dependent on the MTD. Using an optimized MTD and a range of 30 eV the design report value of an uncertainty of 0.1% on the

Table 4.4: Portion of individual systematic effects at different stages of the KATRIN experiment. The portion of an effect at the different stages shows how big the shift of the squared neutrino mass would be relative to the statistical uncertainty if the corresponding effect is neglected. It can be seen that the effects get more influence as the statistical uncertainty decreases. Stage A: Low Statistics, $\sigma_{stat}$ = 10.41 eV$^2$, Stage B: 1eV Sensitivity, $\sigma_{stat}$ = 0.4299 eV$^2$, Stage C: 3 Years, $\sigma_{stat}$ = 0.0368 eV$^2$

| Stage | | Stage A | Stage B | Stage C |
|---|---|---|---|---|
| Effect | syst. shift $\Delta m_\nu^2$ in $10^{-3}$ eV$^2$ | | Portion (%) | |
| transmission function with non-isotropic angular dist. | 12.1 | 0.12 | 2.8 | 32.9 |
| syncrotron radiation | -31.4 | 0.30 | 7.3 | 85.3 |
| thermal doppler effect | -18 | 0.17 | 4.2 | 48.9 |

Table 4.5: Restrictions on the accuracy of parameters at different stages of the KATRIN experiment. Stage A: Low Statistics, $\sigma_{stat}$ = 10.41 eV$^2$, Stage B: 1eV Sensitivity, $\sigma_{stat}$ = 0.4299 eV$^2$, Stage C: 3 Years, $\sigma_{stat}$ = 0.0368 eV$^2$. The parameters have to be known within those limits in order to keep the shift of the squared neutrino mass created by an individual parameter below 10% of the total systematic budget, so the targeted accuracy is $\Delta m_\nu^2 \overset{!}{\leq} 0.1\ \sigma_{stat}$. The systematic budget is given by the statistical uncertainty at different times. The MTD for the 1eV Sensitivity and the 3 years measurement simulations was flat in a range of 60 eV below the endpoint.

| Stage | Stage A | Stage B | Stage C |
|---|---|---|---|
| Parameter | | Accuracy (%) | |
| Column density | $-0.49/+0.43$ | $-0.20/+0.18$ | $-0.016/+0.016$ |
| $B_{Source}$ | $-1.53/+1.31$ | $-0.69/+0.61$ | $-0.061/+0.058$ |
| $B_{max}$ | $-1.24/+1.48$ | $-0.50/+0.57$ | $-0.047/+0.050$ |
| $B_{ana}$ | $\sim \pm 40$ | $-1.71/+1.55$ | $-0.14/+0.14$ |
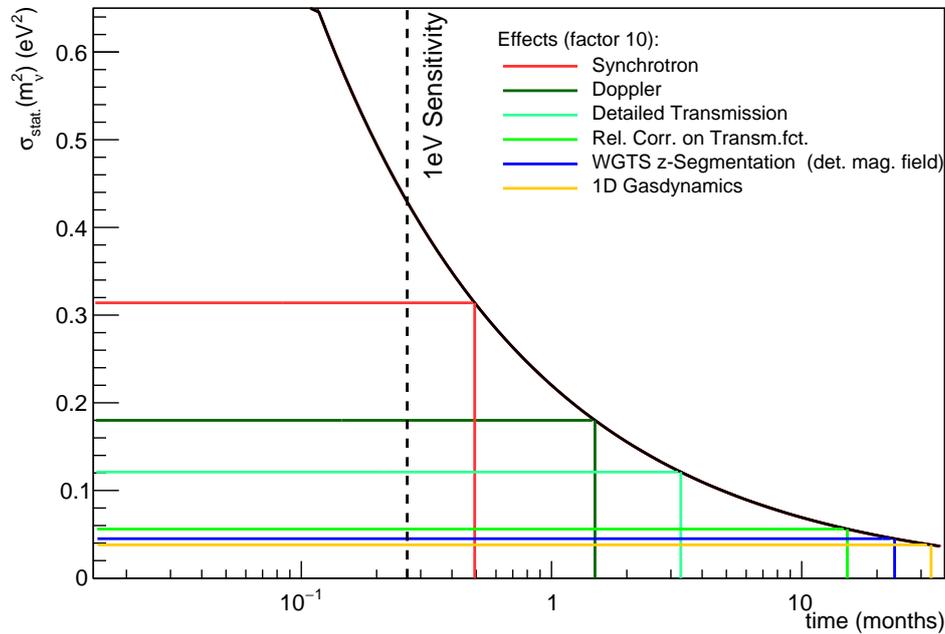
Figure 4.3: The statistical uncertainty $\sigma_{stat}$ as a function of measuring time. The graph shows at which times a systematic effect reaches 10% of the statistical uncertainty.

column density in order to keep the systematic shift at about 10% of the statistical uncertainty can be reproduced, while for a flat distribution in the range of 30 eV the requirement gets more stringent to about 0.08%. Compared to the requirement of 0.016% using a flat distribution in a range of 60 eV or 0.019% using an optimized MTD in a range of 60 eV this is a significant improvement.
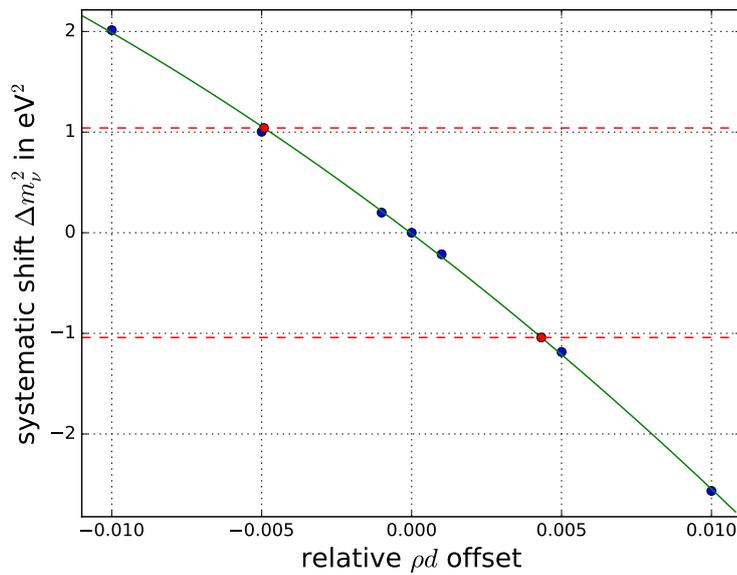
Figure 4.4: Systematic shift of the squared neutrino mass as a function of the of the column density offset. The x-axis is the relative deviance of the column density from the model value. The y-axis is the shift of the squared neutrino mass if the wrong model value is used for fitting. By setting a limit for a maximally allowed neutrino mass shift the accuracy at which the column density needs to be known can be determined.

# Chapter 5

# First Tritium data

This chapter serves as an overview of the methods that are used to analyze the data and to present a first look at the data. In the end of May and early June 2018 KATRIN took first data with tritium during two separate campaigns, namely the Very First Tritium and the First Tritium campaign. Besides testing the whole data processing and analysis chain one goal was also to gain first results of the fitting parameters. One big endeavor of the First Tritium campaign was to check stability conditions. As shown in table 4.5 it is of utmost importance to keep the control parameters of the system stable and to have low uncertainties on the control parameters in order to reduce systematic effects.

## 5.1 First look at the data

As demonstrated in section 4.2.1 the sensitivity on the neutrino mass is rather limited for First Tritium. For this reason the neutrino mass was fixed to zero and the focus was on the other fit parameters endpoint, signal rate and background rate. The actual observable in KATRIN is a so-called effective endpoint, which is related to the true endpoint by an additional factor. This factor is given by the difference of the work functions of the source and the spectrometer and tritium plasma effects in the source. This applies to all endpoint results shown in this chapter.

### 5.1.1 Very First Tritium

During May 2018 tritium was fed into the WGTS for the very first time. Because of the low tritium density it is not possible to have a stable amount of $T_2$ molecules

so instead only DT molecules were used as source material. The campaign consists of eight tritium scans that can be separated into different categories. The first four scans were performed with a tritium purity of 0.9%, the other four scans with a purity of 1.2%. For each of those two sets respectively the first two scans had stable conditions while during the latter two some parameters related to the gas pressure were declining. The reason for this is that during Very First Tritium the gas was not actually circulated in the inner loop system. Instead gas containers, so-called gas mice, were attached to the WGTS. The gas was fed into the source and steadily pumped out at the two open ends of the WGTS without being fed back into the source. As a result the gas density, pressure and composition could be held at a constant level for the time of about two runs. After that those parameters started to decline. A final separation can be made by looking at the scan direction. For each block of stable and unstable runs, each consisting of two runs respectively, there is one scan up and one scan down. The scan direction is defined by the order of retarding potentials. A scan starting at a retarding potential below the endpoint and then subsequently going towards the endpoint, thereby decreasing the measured rate until it exceeds the endpoint is called 'scan up'. Starting above the endpoint and going down, thereby increasing the count rate is called 'scan down'. In both cases there are measuring points above the endpoint, where no electrons originating from tritium $\beta$-decay are expected. Those points are important for the determination of the background rate. The runs of the Very First Tritium campaign are shown in table 5.1.

The plots in fig. 5.1 and 5.2 are showing the fits and residuals of the very first scan (run 40257) with tritium. This run was a scan down and had stable conditions and a tritium purity of 0.9%. In fig. 5.1 only data inside a range of 200 eV below the endpoint was considered. Fig. 5.2 shows the fit of the full measured range down to 2 keV below the endpoint. Looking at the residuals of the fits it can be seen that even though there is only very limited statistics the model works very well with the given data.

Because of the low statistics collected within those very first measurements, the purpose was more to test the whole data processing and data analysis chain than to actually gain meaningful results of the fitting parameters. The fits that were performed serve as a comparison between the different fitters and the fitting ranges.

Table 5.1: Overview of the runs in Very First Tritium. The runs can be divided by tritium purity, stability and scanning direction.

| Run number | DT (%) | stability | Scan direction |
|:---:|:---:|:---:|:---:|
| 40257 | 0.9 | stable | down |
| 40258 | 0.9 | stable | up |
| 40259 | 0.9 | instable | down |
| 40260 | 0.9 | instable | up |
| 40263 | 1.2 | stable | down |
| 40264 | 1.2 | stable | up |
| 40265 | 1.2 | instable | down |
| 40266 | 1.2 | instable | up |
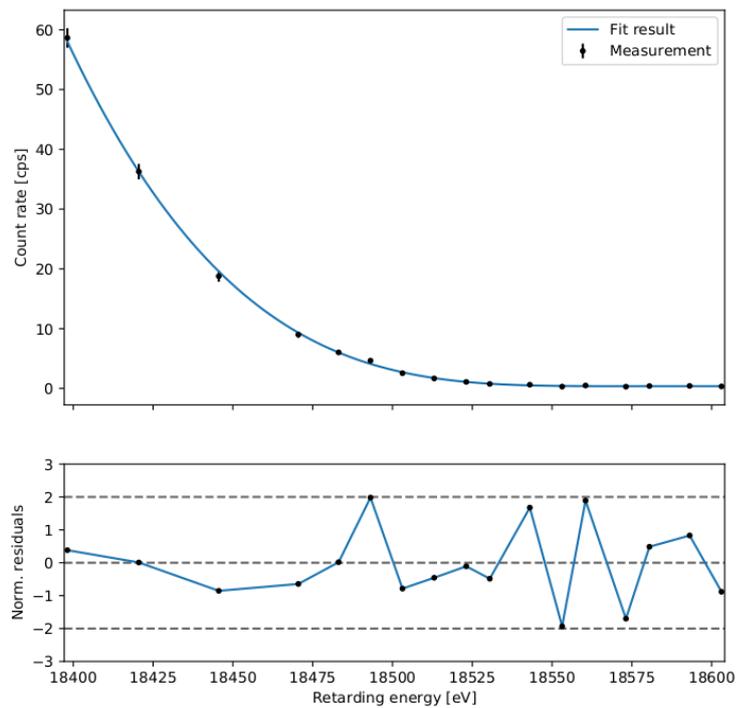


Figure 5.1: Fit of the very first scan with tritium (40257). For the fit only the data in the last 200 eV below the endpoint are considered.
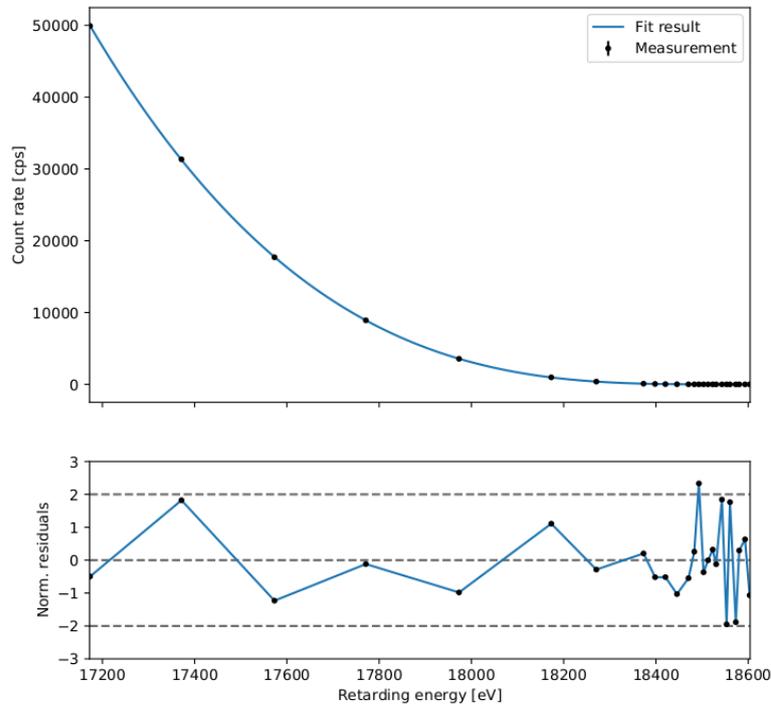
Figure 5.2: Fit of the very first scan with tritium (40257). For this fit the entire measured range of 2 keV below the endpoint was considered.

Tables 5.2 and 5.3 show the results of run 40257 and run 40263 of the Very First Tritium campaign, performed with Fitrium. Run 40263 was a scan down with stable conditions and a tritium purity of 1.2%.

### 5.1.2 First Tritium

After some preparations the First Tritium campaign followed in the first half of June 2018. This campaign consists of many scans with tritium that can be divided into different categories shown in table 5.4. Those runs are just the standard scans. Not shown in the table are special runs used as stability-, background- or sterile neutrino measurements.

Table 5.2: Fit results of the runs 40257 and 40263. Both fits were performed using only the data of the last 200 eV below the endpoint.

| Run number | $E_0$ (eV) | Norm | Bg (mcps) | $\chi^2$/ndof |
|:---:|:---:|:---:|:---:|:---:|
| 40257 | $18575.1 \pm 1.5$ | $0.93 \pm 0.04$ | 380 +22 -21 | 21.047/15 |
| 40263 | $18573.0 \pm 1.2$ | $1.03 \pm 0.04$ | $409 \pm 22$ | 15.041/15 |

Table 5.3: Fit results of the runs 40257 and 40263. Both fits were performed using the full measured range of 2 keV below the endpoint.

| Run number | $E_0$ (eV) | Norm | Bg (mcps) | $\chi^2$/ndof |
|:---:|:---:|:---:|:---:|:---:|
| 40257 | $18573.3 \pm 0.4$ | $0.997 \pm 0.001$ | $387 \pm 20$ | 30.713/23 |
| 40263 | $18573.4 \pm 0.3$ | $1.011 \pm 0.001$ | 408 +21 -20 | 26.288/23 |

Table 5.4: Overview of the runs in First Tritium. The runs can be divided by run duration, column density $\rho$d and scanning direction.

| Run numbers | Run time (h) | $\rho$d ($10^{21}$ 1/m$^2$) | relative $\rho$d (%) | Scan direction |
|:---:|:---:|:---:|:---:|:---:|
| 40531 - 40543 | 1 | 4.45 | 100 | up/down |
| 40603 - 40613 | 1 | 4.45 | 100 | up/down |
| 40667 - 40693 | 3 | 4.45 | 100 | up/down |
| 40763 - 40766 | 1 | 2.14 | ∼47 | up/down |
| 40794 - 40805 | 1 | 1.08 | ∼23 | up/down |
| 40926 - 40935 | 1 | 3.20 | ∼70 | up/down |
| 40976 - 40998 | 1 | 4.45 | 100 | up/down |
| 41001 - 41031 | 1 | 4.45 | 100 | up/down/ random |

The 27 runs with a total measuring time of 3h each at full column density are mainly used for fit parameter determination. The runs with reduced column density and the runs with a random scan direction were mainly performed in order to investigate systematic effects.

There are different types of fits that are defined in the following way:

- **Uniform fit:** In a uniform fit the statistics of all 148 pixels are combined by treating the whole detector as one big pixel. For performing a uniform fit only one single model is used. All pixel dependent parameters get averaged over the whole detector and get incorporated in the model as a single value. The counts of all pixels get summed up for each retarding potential. The uniform fit allows to exclude pixels. In this case the excluded pixels are ignored and the parameters get averaged over the remaining pixels.

- **Single Pixel fit:** In a single pixel fit only the counts of a pixel at different retarding potentials are used and fitted to a model corresponding to this pixel. Fitrium allows to set ranges of pixels or exclude certain pixels from a fit. If a fit is performed, only the selected pixels are fitted and the fit results are obtained for every single pixel individually.

- **Multi Pixel fit:** The multi pixel fit is similar to the single pixel fit. Only a selected set of pixels is fitted. The fit parameters are divided into pixel dependent and physical parameters. The signal rate and the background rate can be different from pixel to pixel. That is why those parameters are fitted independently for every pixel. Physical quantities like the endpoint and the neutrino mass should be the same for every pixel or respectively the spectrum of each pixel. So instead of using an independent model for each pixel with 4 fit parameters, the likelihood will be minimized with respect to the two pixel dependent parameters background and signal rate and one common endpoint and neutrino mass.

- **Combined fit:** A combined fit can be performed for a selected set of runs. This can be done for either of the three fitting types above. A combined fit averages the control parameters over the selected set of runs and uses this number to create one single model. Of course this can only be done if the control parameters are stable within those runs. All runs are fitted with one

common model, so if in one of the runs one parameter differs too much from the others, the averaged value will be influenced and the selected block of runs is fitted with a wrong model, which leads to systematic errors on the fit parameters. Besides the requirement of stability of the control parameters, the precision of the retarding potential is also an issue. During runs with the same MTD, the voltage is set on the same retarding potentials. In reality the voltage is usually not hitting the exact same voltage between runs. Around each measuring potential is a very small spread of voltages. In a combined fit all voltages are treated as several measuring points. Some of them are even less than 1 mV away from each other.

- **Stacked fit:** A stacked fit is basically the same as a combined fit with one difference. As explained above the spread of voltages around each of the retarding potentials is usually very small. If the spread around the mean value of the voltage is small enough, the runs can be stacked. That means the counts of all runs are summed up at each mean retarding potential and are then fitted with a common model. A spread can be considered as small enough if the systematic error that is induced by averaging the voltages is not significant with respect to the total systematic budget.

The fits of Very First Tritium data in fig. 5.1 and 5.2 were examples of uniform fits. A combined uniform fit of the runs 40531 to 40693 can be seen in fig. 5.3. In all fits the pixels of the outer two rings of the detector are excluded since they did not show a significant count rate, assumingly the electrons created near the source walls are blocked somewhere along the 70 m long beam line. Also a small number of pixels on one side of the detector are excluded which were covered by the Forward Beam Monitor (FBM) that is positioned at the end of the transport section and is used for monitoring the rate stability.

### 5.1.3 Correlations

Parameters for which correlations might be expected include the normalization, the endpoint, the column density and the tritium purity. The tritium purity or DT-concentration directly influences the signal rate, which in turn can have influence on the endpoint of the spectrum. The influence of the column density is more subtle.
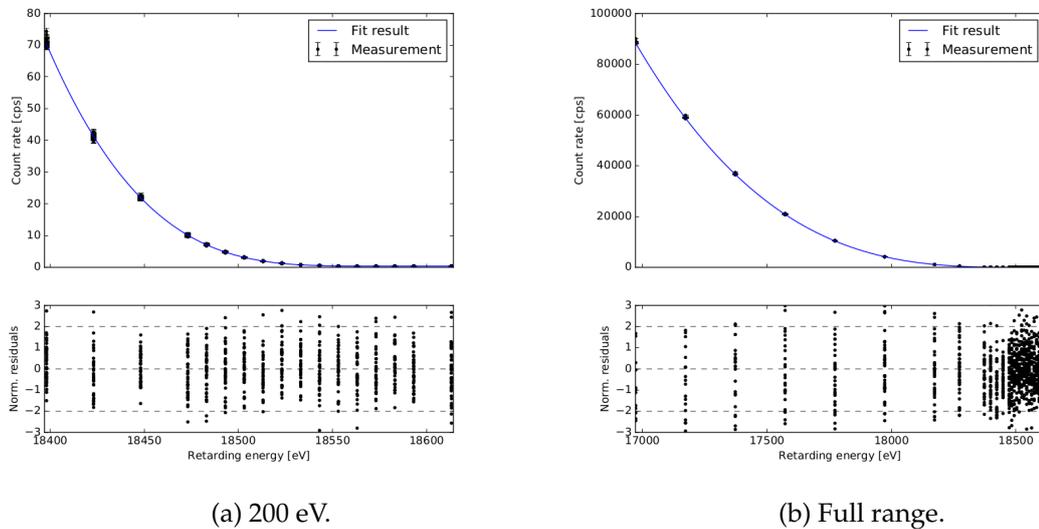
(a) 200 eV.

(b) Full range.

Figure 5.3: Fit of the data of (a) the first 200 eV and (b) the full range of all tritium scans within the range of runs 40531 to 40693 combined. The control parameters of all pixels and all runs are averaged to one single model that is used for fitting all the data.

The higher the column density, the more decays happen in a source segment but simultaneously the scattering probability increases. This mainly effects the response function. The shape of the response function in turn has a very high influence on the final spectrum shape. Fig. 5.4 to 5.8 show the plots of the correlations that are investigated. For those plots all runs of first tritium are used. It has to be considered that the number of data points is limited in First Tritium and therefore it is rather difficult to draw meaningful conclusions from it.

There seem to be no correlations except between the normalization and the DT concentration. The anticorrelation between them shows up when looking only at the runs that were performed at 100% column density (fig. 5.8), but the structure can already be seen in the plot including all runs (fig. 5.7). The determination of the DT concentration is based on Laser Raman Spectroscopy [43] and an updated determination of the DT concentrations of all runs is work in progress. The correlation might disappear with the updated values of the gas compositions.
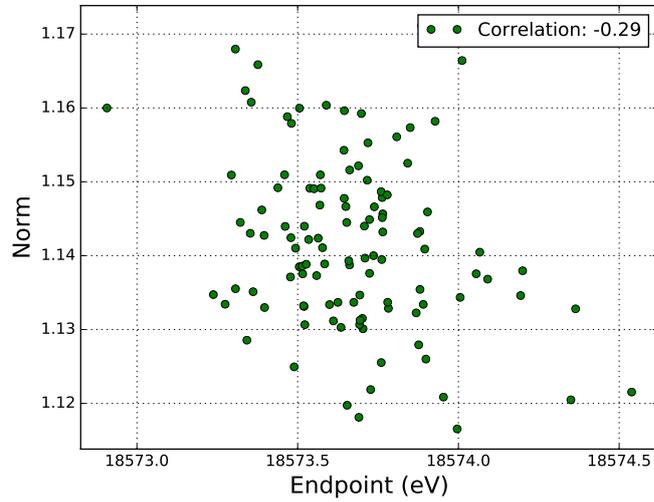
Figure 5.4: Correlation plot of the normalization and the endpoint. They seem rather uncorrelated with each other.
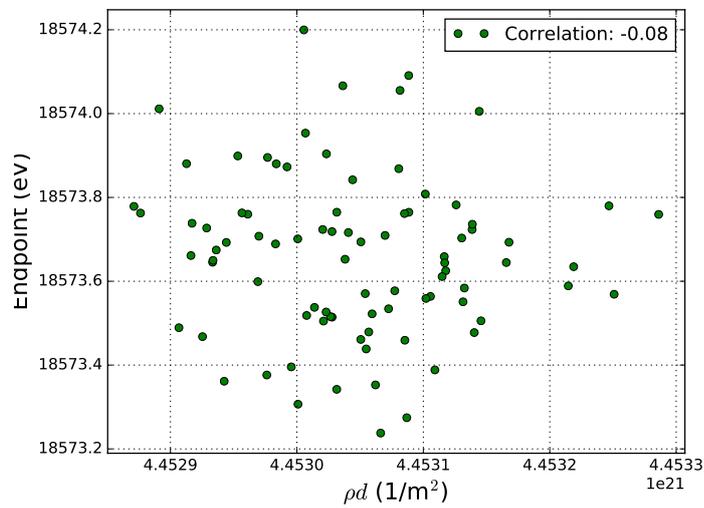


Figure 5.5: Correlation plot of the endpoint and the column density. There is no correlation visible.
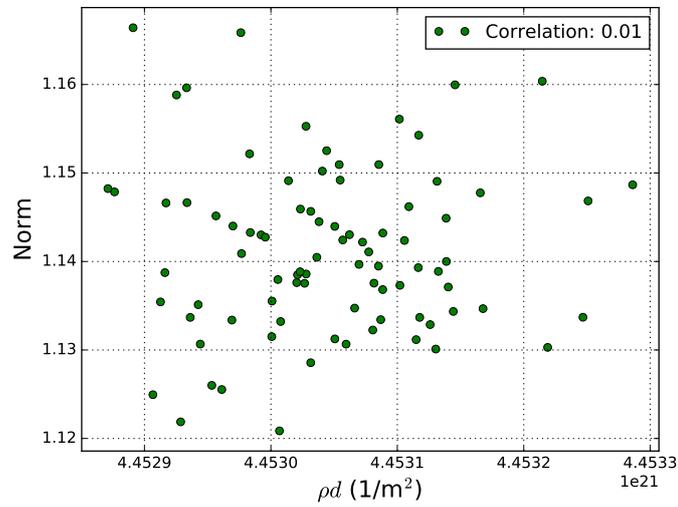
Figure 5.6: Correlation plot of the normalization and the column density. There is no correlation visible.
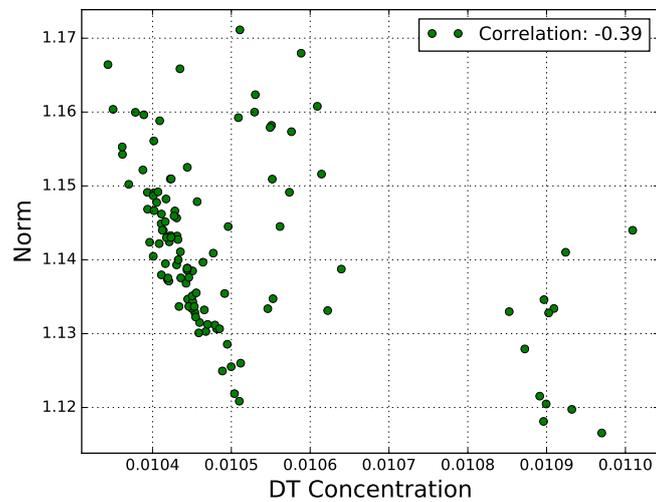


Figure 5.7: Correlation plot of the normalization and the DT concentration. It seems that the normalization is moderately correlated to the DT concentration. This plot includes the data points of all First Tritium runs. There is a substructure visible, which corresponds to all runs at full column density, which can be seen in fig. 5.8.
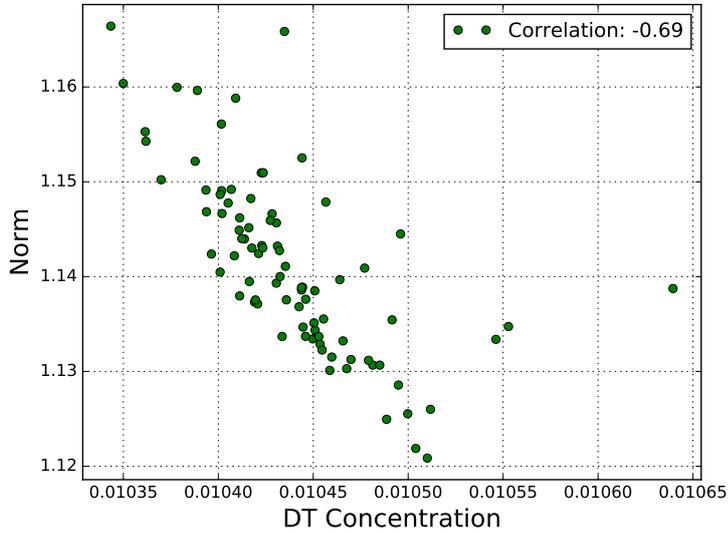
Figure 5.8: Correlation plot of the normalization and the column density. While in fig. 5.7 all runs of First Tritium are included, for this plot all runs with reduced column density are excluded. An anticorrelation appears between the normalization and the DT concentration.

## 5.2 Parameter evolution

Another way of detecting system instabilities or revealing scans that show salient behaviour is to check the overall evolution of the fit parameters over all runs. This has been done for all small range (200 eV below endpoint) and full range fits (2 keV). Fig. 5.9 to 5.11 show the fit parameter evolution of the uniform fit results of both fitting ranges. Table 5.5 summarizes the mean fit results and their standard deviation.

Table 5.5: Mean of the fit results of all runs in two different ranges (small range = 200 eV below endpoint, full range = 2 keV below endpoint).

| Fitting range | $E_0$ (eV) | Norm | Bg (mcps) |
|:---:|:---:|:---:|:---:|
| small range | $18573.8 \pm 0.9$ | $1.13 \pm 0.03$ | $395 \pm 18$ |
| full range | $18573.7 \pm 0.2$ | $1.142 \pm 0.011$ | $395 \pm 16$ |
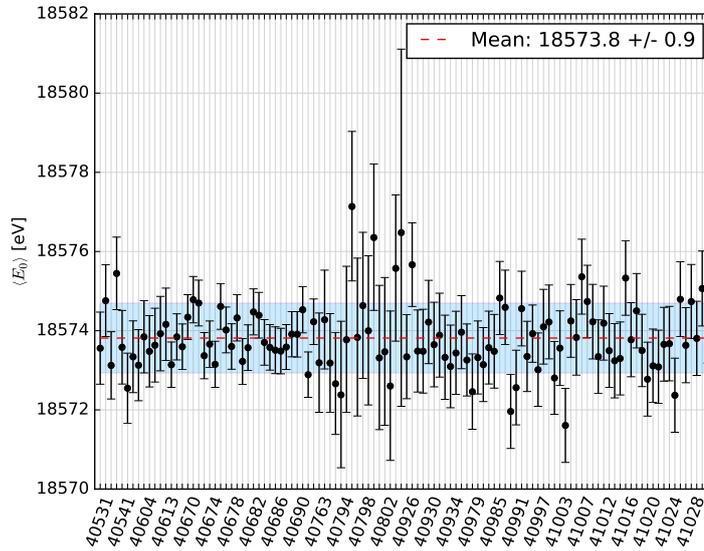
(a) Evolution of the endpoint fit result over all runs in the small range (200 eV below endpoint).
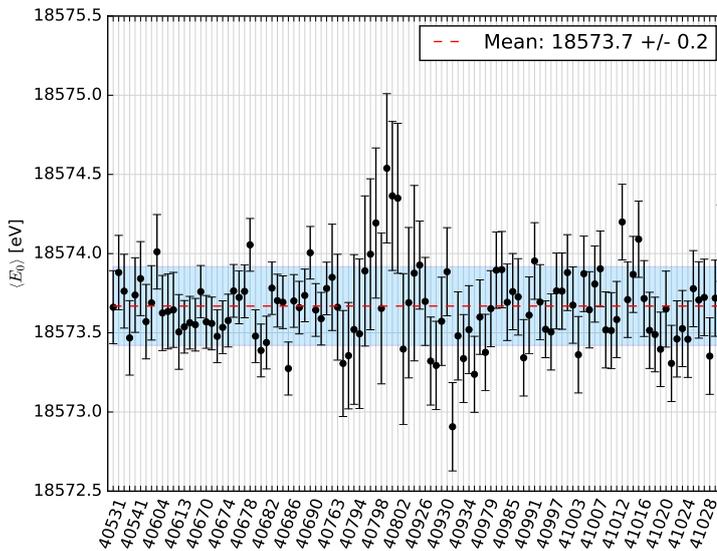


(b) Evolution of the endpoint fit result over all runs in the full range (2 keV below endpoint).

Figure 5.9: Evolution of the fit result of the endpoint over all uniform fits. (a) small range and (b) full range. The fit results look very stable in both ranges.
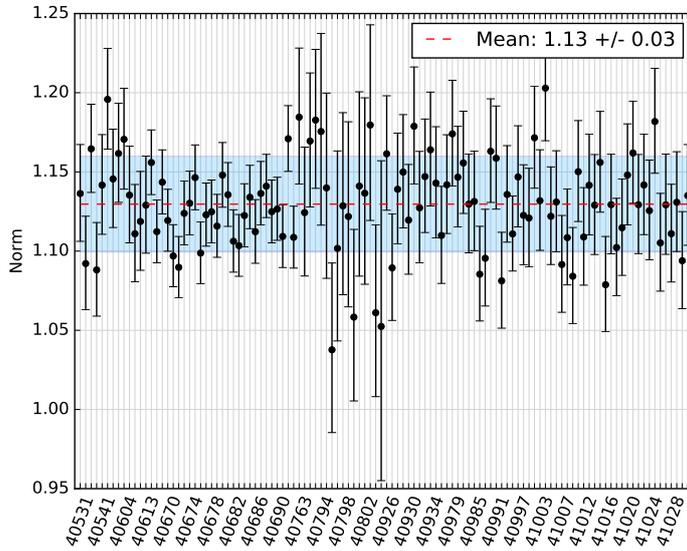
(a) Evolution of the normalization fit result over all runs in the small range (200 eV below endpoint).
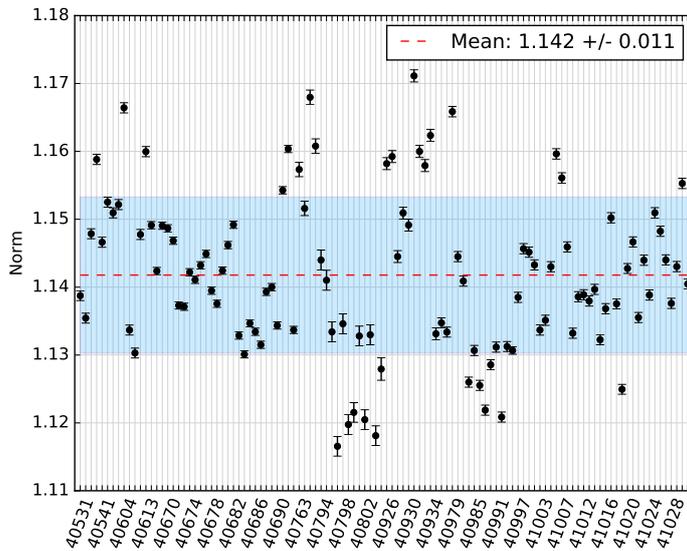


(b) Evolution of the normalization fit results over all runs in the full range (2 keV below endpoint).

Figure 5.10: Evolution of the fit result of the normalization over all uniform fits. (a) small range and (b) full range. The fit results look very stable in the short range. The spread of results in the long range is a consequence of the fit using statistics only. Including systematic effects increases the error bars and gives a similar picture as in the short range.
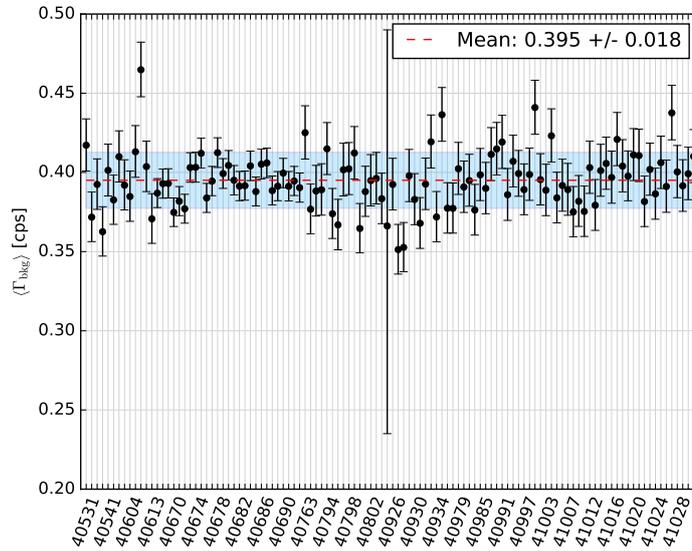
(a) Evolution of the background fit results over all runs in the small range (200 eV below endpoint).
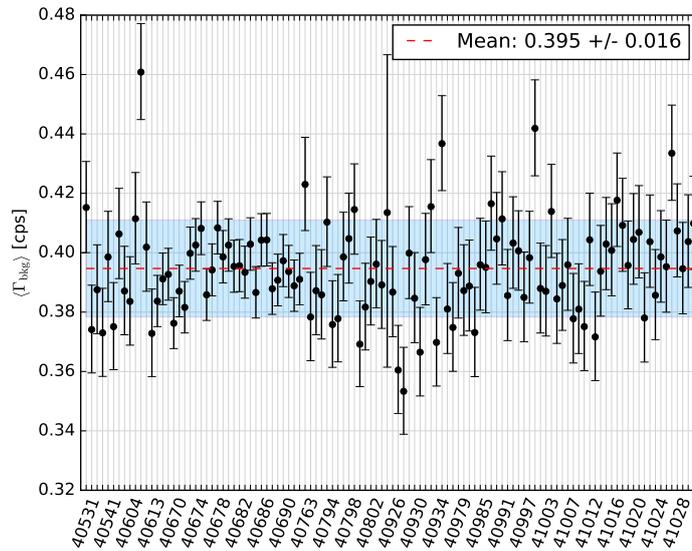


(b) Evolution of the background fit results over all runs in the full range (2 keV below endpoint).

Figure 5.11: Evolution of the fit result of the background rate over all uniform fits. (a) small range and (b) full range. The fit results look very stable in both ranges.

The plots show the stability of the fit parameters over all runs within their standard deviation. In the range of the runs 40763 to 40935 some fluctuations and larger error bars can be seen especially for the endpoint and normalization fit results. This is the range of runs that were performed with a lower column density. The spread of the fit results of the normalization in the full range (fig. 5.10b) is a consequence of the fit using statistics only. Including systematic effects, especially the fluctuations of the DT concentration, increases the error bars and creates a similar picture as in the short range. The mean fit results displayed in the plots and summarized in table 5.5 show very good agreement between the two fitting ranges.

# Chapter 6

# Column density determination

In the first part of this chapter different methods that are used to determine the column density are presented and some results are shown. Afterwards some systematic effects that affect the column density are presented. The column density has direct influence on the scattering probabilities $P_i$ in equation 3.7 an thus has direct influence on the response function. The column density is a critical parameter regarding the systematic uncertainty since even small changes in the response function have significant impact on the shape of the integrated spectrum. As shown in table 4.5 the column density has to be known to a very precise level at all stages of the experiment. For this reason the KATRIN experiment uses an angular selective electron gun (in the following called e-gun). The e-gun can produce mono-energetic electron beams that can be emitted under different angles from the rear side of the WGTS. With the knowlegde of energy as well as starting angle of the electrons the response function and the column density can be determined to a very high precision.

The e-gun was very recently successfully installed and can be used for future measurements to determine the column density. However the e-gun was not yet available during the First Tritium campaign. The uncertainty of the column density is a non negligible contributor to the systematic uncertainty of First Tritium fit results. For this reason other ways of determining the column density were needed.

There are two different approaches to determining the column density. The first approach is a direct calculation from other control parameters related to the column density such as the buffer vessel pressure or the throughput of the source gas [44]. The calculated values are also the ones that are used in the run summary. A run summary is a file containing all necessary information about a run, including the
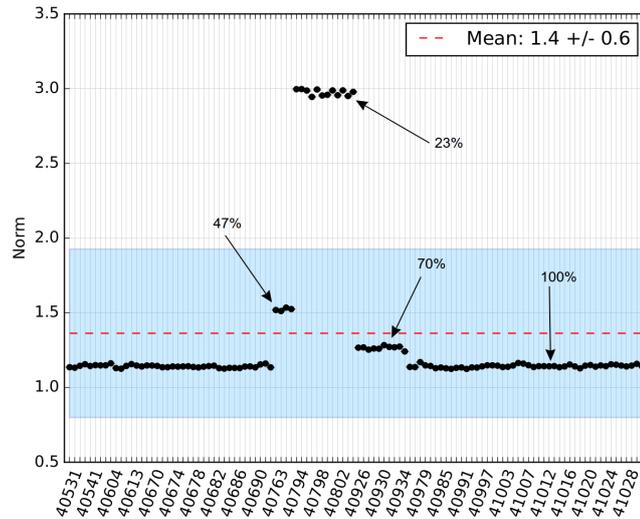
Figure 6.1: The evolution of the normalization over all runs, using a wrong value for the column density. The percentage indicates the column density relative to the standard value used during First tritium. This is an example of how checking the stability of the fit parameters can reveal issues that will eventually lead to an improvement of the model.

values of control parameters as well as the MTD and counts per pixel. The other approach is to try to get information directly from the data by considering the column density not as a control parameter but as an observable. In the end both ways can be compared and verified if they yield the same results.

The calculated values of the column density were updated several times. The first calculations, using the buffervessel pressure turned out to not give the correct results. This could be seen well in the evolution of the fit parameters, especially in the endpoint and the normalization. Fig. 6.1 shows the evolution of the fitted normalization using the incorrect value of the column density for the fitting model.

This example shows how checking the stability of parameters can help detecting errors in the modeling or fitting of the data. The updated calculations of the column density lead to a stable value of the normalization like it is shown in fig. 5.10.

Additionally this shows that the calculations of the column density are not necessarily completely correct and a different method to obtain the column density is needed.

## 6.1 Methods to obtain information from the data

The focus in this thesis lies on the determination using data. This can be done in two different manners. First by setting the column density as a fit parameter. To be more specific the actual fit parameter is the product of the column density and the scattering cross section. This product goes into the scattering probabilities and can be fitted. At the time those studies were done this was computationaly very time consuming since the response function had to be exactly calculated at every point. Furthermore the minimization with respect to the column density was solely based on function evalutations. Today the fit makes use of the analytical derivative of the column density which is much faster. The other way is to perform a manual fit by scanning the parameter space by performing several fits with different column densities and finding a minimum in the negative log-likelihood of the fit. The advantage of this method is that it was considerably faster than a fit at that time because the response function can be approximated. As a verification a comparison of both methods yields the same result within their uncertainty.

### 6.1.1 Scan results compared to calculations

Comparing the results of the scans or respectively the fits of the column density to the calculated values shows some discrepancies that can be seen in fig. 6.2.

The scans for this plot were all performed with the full range and no systematics. As will be shown in the next section, the result of the fits and scans is very range dependent. Using the full range for fitting the column density gives values lower than the calculated ones, fitting in the short range results in higher values. This is not yet fully understood and gives a hint that the model that is used is imperfect, especially in the region deep in the spectrum some approximations are made. However by including systematic effects (sec. 6.2) this behaviour gets damped.

### 6.1.2 Scan results compared to calculations at reduced column density

After the block of 3h runs the column density was lowered to $\sim$ 47%, then to $\sim$ 23% and after that increased to $\sim$ 70% and eventually increased back to 100% (see table 5.4). Fig. 6.3 to 6.5 are showing the column density scans for all runs of each block combined.
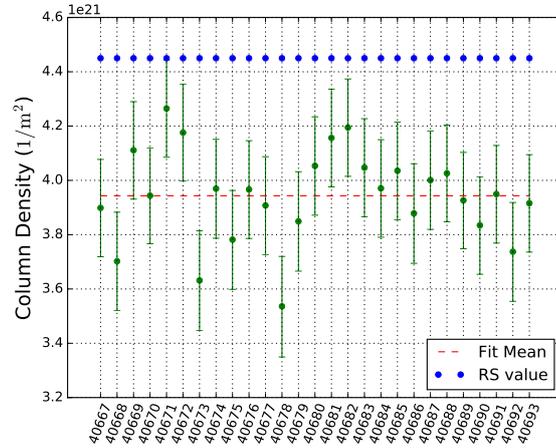
Figure 6.2: The scan results of the column density (green) of all 3h runs and their mean value (red). The blue values are the calculated values in the run summary.
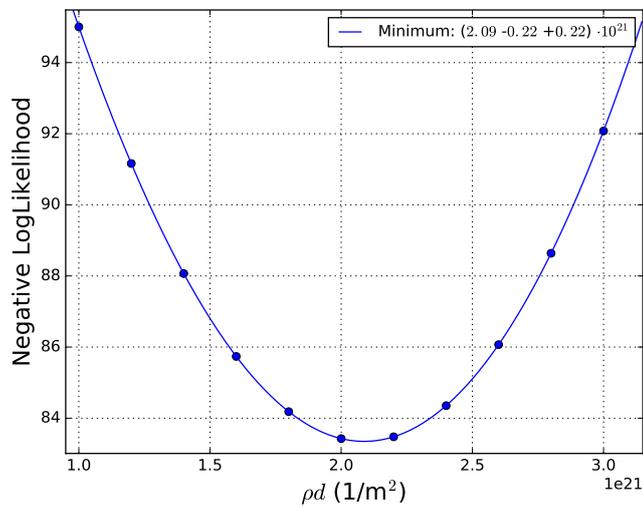


Figure 6.3: Column density scan of the runs 40763 to 40766 combined. This block of runs was performed with about 47% of the standard column density.
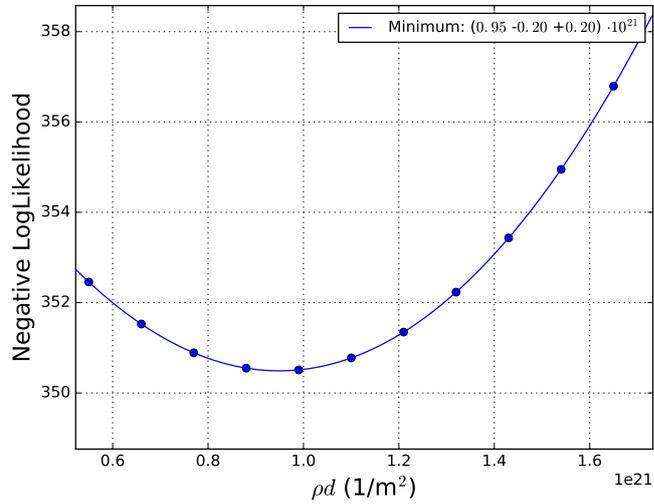
Figure 6.4: Column density scan of the runs 40794 to 40805 combined. This block of runs was performed with about 23% of the standard column density.
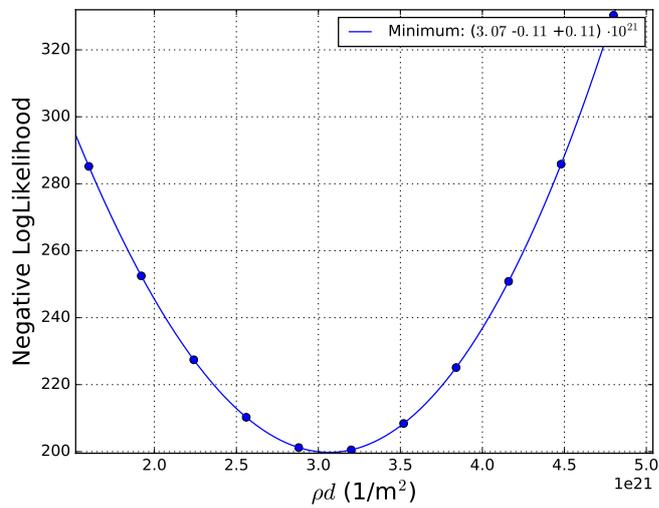


Figure 6.5: Column density scan of the runs 40926 to 40935 combined. This block of runs was performed with about 70% of the standard column density.

Table 6.1: Comparison of the scan results with the calculated values reveals that for the scans with reduced column density the results are in very good agreement within their uncertainties.

| | 47% $\rho d$ ($10^{21}$ 1/m$^2$) | 23% $\rho d$ ($10^{21}$ 1/m$^2$) | 70% $\rho d$ ($10^{21}$ 1/m$^2$) |
|---|---|---|---|
| Scan result | $2.09 \pm 0.22$ | $0.95 \pm 0.20$ | $3.07 \pm 0.11$ |
| Calculation | $2.14 \pm 0.21$ | $1.08 \pm 0.11$ | $3.20 \pm 0.32$ |

Table 6.1 contains the scan results and the calculated values of the run summary for comparison. They are in very good agreement within their uncertainties.

## 6.2 Systematic uncertainties

Looking at fits of the column density using different fitting ranges it becomes apparent that there is a strong range dependence of the result. For this study only the 3h runs are used. The column density is fitted individually for every run in 6 different ranges: -1600 eV, -1000 eV, -600 eV, -400 eV, -300 eV and -200 eV below the endpoint. Then the mean of all fit results at every fitting range is taken. In fig. 6.6 some selected individual runs can be seen. Most of them already show a general upward trend of the fit result of the column density with decreasing fitting range. Fig. 6.7 contains the distribution of fit results of all 3h runs at each of the six fitting ranges. Here the increase of the fit result can clearly be seen. The result also exceeds the calculated value of $4.45 \cdot 10^{21}$ 1/m$^2$ already in the -1000 eV range. In the following some systematic effects were implemented into Fitrium step by step to check their influence on the fit results of the column density. Those effects include an energy dependent inelastic cross section, an energy dependent detector efficiency and fluctuations of the DT concentration.

### 6.2.1 Energy dependent cross section

During the full 3 year KATRIN measurement phase the measuring time distributions cover just a small range below the endpoint down to maximally -60 eV below the endpoint. In this energy range the inelastic cross section of electrons scattering off source gas is approximately constant which is used in the model for calculating the
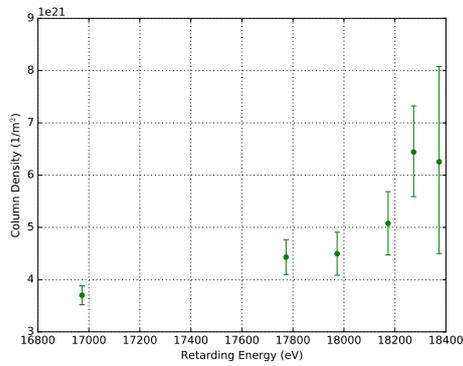
(a) Run 40668.
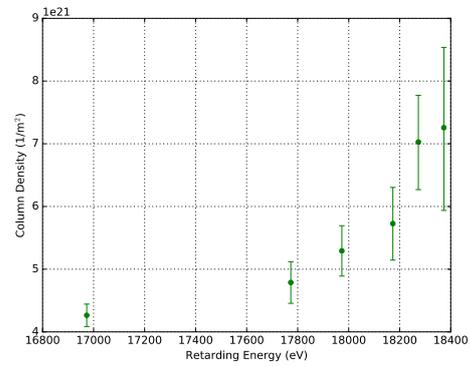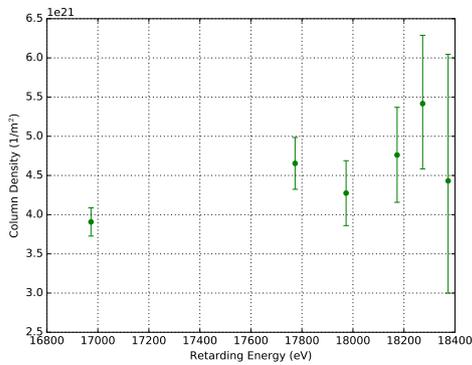
(b) Run 40671.

(c) Run 40677.
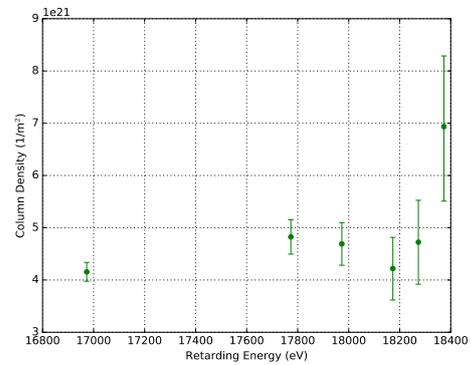
(d) Run 40681.
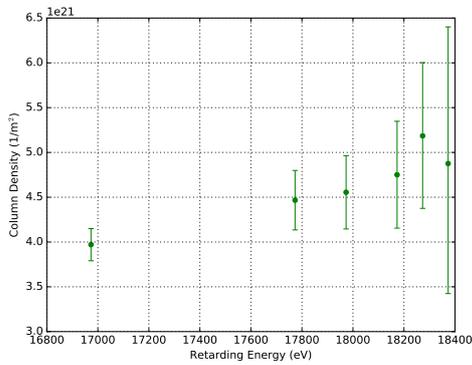
(e) Run 40684.
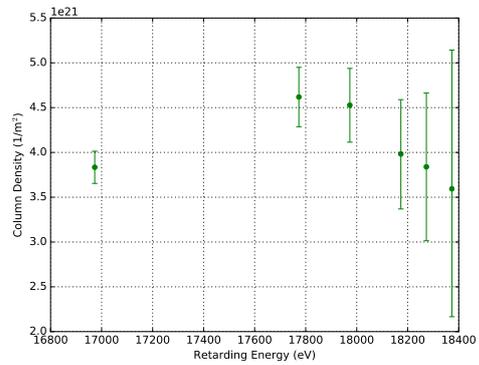
(f) Run 40690.

Figure 6.6: Some of the individual runs and their fit results of the column density in $1/m^2$ at the six different fitting ranges -1600 eV, -1000 eV, -600 eV, -400 eV, -300 eV and -200 eV below the endpoint. Most of the runs already show a general upward trend with a decreasing fitting range.

(a) -1600 eV below endpoint.

(b) -1000 eV below endpoint.

(c) -600 eV below endpoint.

(d) -400 eV below endpoint.

(e) -300 eV below endpoint.

(f) -200 eV below endpoint.
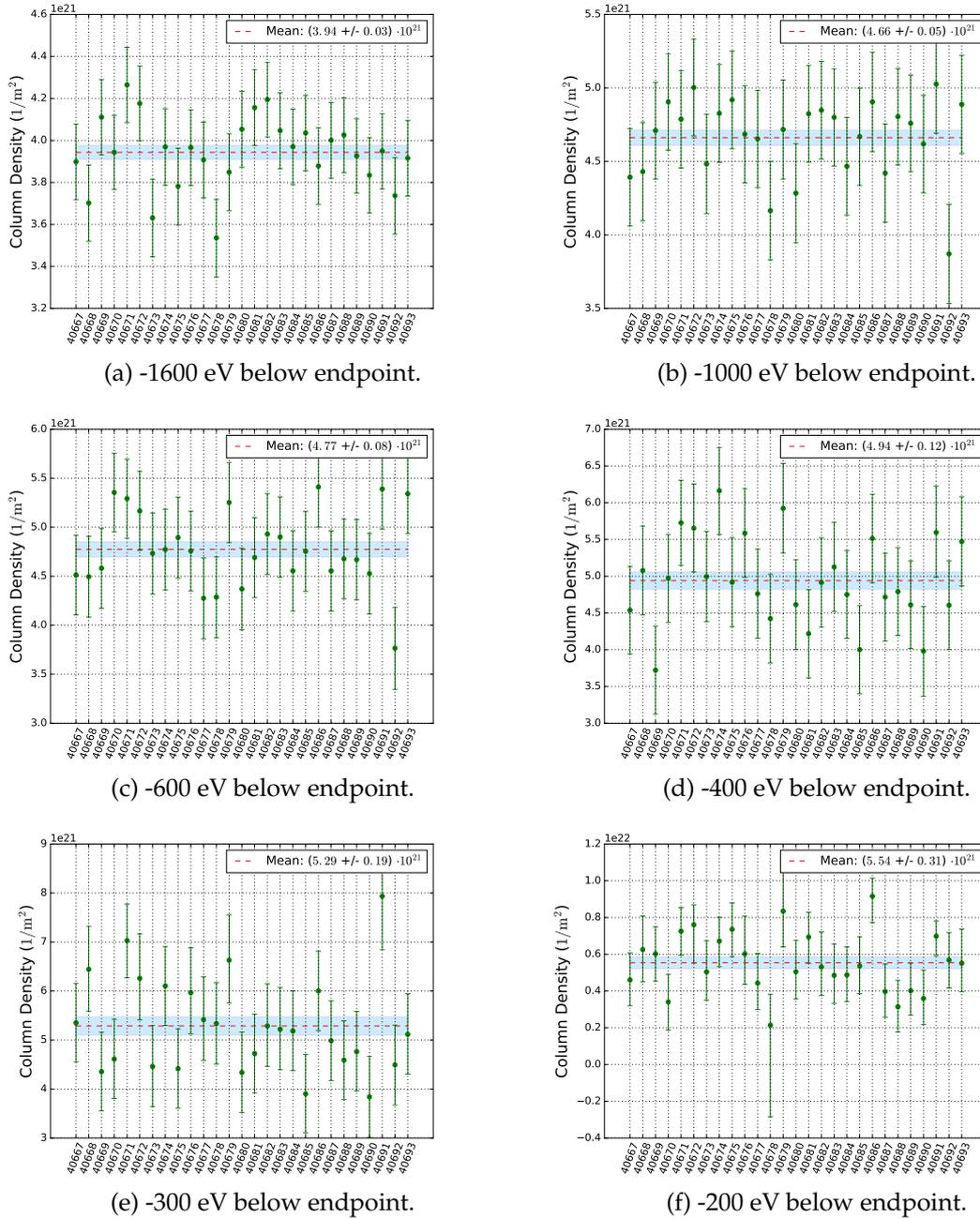
Figure 6.7: Distribution of fit results of all 3h runs at each of the six different fitting ranges. The increase of the value of the fit result with decreasing data range can clearly be seen.

scattering probabilities. By going deeper into the spectrum however the effect of a non constant cross section becomes noticable. The full equation for the total inelastic cross section $\sigma_{tot}$ for collisions of $H_2$ with fast charged particles was calculated in [45]. In the case of a relativistic incident particle it results in:

$$\sigma_{tot} = \frac{4\pi a_0^2 z^2}{E/R} \left[ 1.5487 \ln \left( \frac{\beta^2}{1-\beta^2} \right) + (17.4615 \pm 0.0434) \right] \qquad (6.1)$$

With the Bohr radius $a_0$, the Rydberg energy $R$, the charge of the incident particle $z$ (=1 for electrons), the kinetic energy of the electron $E$ and the velocity of the electron $\beta = \frac{v}{c}$. The energy dependence of the cross section can be seen in fig. 6.8 together with a comparison to the constant value that was previously used in the model. The green area indicates the typical range in which measurements will be performed during the standard neutrino mass measurements. In this range the cross section can be approximated as a constant value.

The influence on the fit result of the column density in the different ranges can be seen in fig. 6.11. The result of the column density gets increased in the larger fitting ranges, flattening the whole structure slightly. The result is still very range dependent and more systematic effects need to be added.

### 6.2.2 Energy dependent detector efficiency

Another systematic effect arises from the energy dependence of the detector efficiency that was not used in the model prior to First Tritium as the effect is very small in the usual measuring range which can be seen in fig. 6.9. There are three energy dependent effects influencing the detector efficiency. The smallest efficiency loss comes from pile-up in the detector. Another efficiency loss is caused by backscattering of electrons. Finally the choice of the region of interest influences the detector efficiency [46]. The function for the energy dependence in fig. 6.9 comes from a fit of empirical data.

Including this effect in the fits of the column density improves the result especially deeper in the spectrum, which can be seen in fig. 6.11. But the range dependence is still present and the fit results are now all above the calculated value. Further systematic effects need to be included. In the next steps covariance matrices will
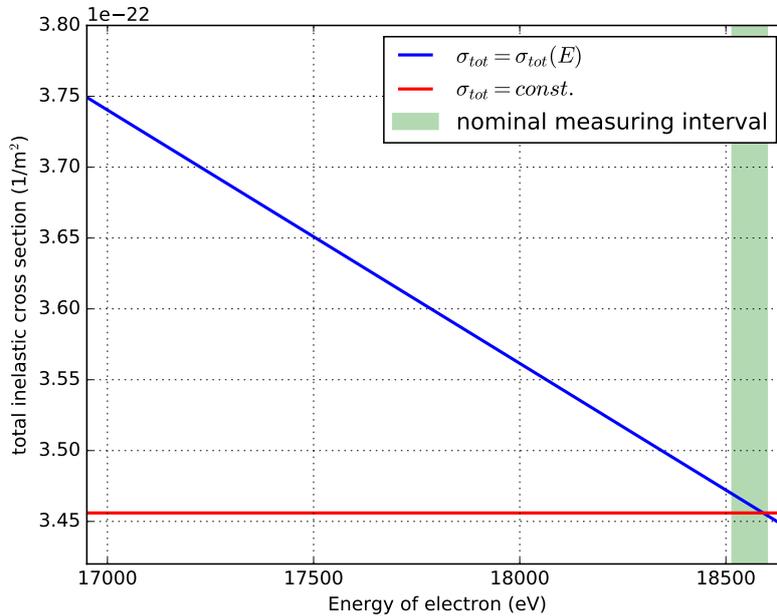
Figure 6.8: Energy dependent total inelastic cross section (blue) together with the previously used constant value (red). Within the typical measuring range (green) the approximation to a constant value is accurate enough, differing only by 0.4% at 60 eV below the endpoint.

be used to describe fluctuations of the tritium purity and put uncertainties on the magnetic fields and the description of the final states.

### 6.2.3  Tritium purity fluctuations

The DT concentration of the source was very stable, fluctuating only within an uncertainty of about 0.1% [47]. These fluctuations were incorporated into a chi-squared fit via a fractional covariance matrix that was added to the statistical uncertainty matrix. The DT fluctuation matrix can be seen in fig. 6.10. The tritium fluctuations are uncorrelated between the measuring points leading to the matrix just having entries on the diagonal elements.

   The effect on the fitting results is minor, as can be seen in fig. 6.11. Adding covariance matrices with uncertainties for the magnetic fields and the description of the FSD might improve the results. The ongoing measurements with the electron
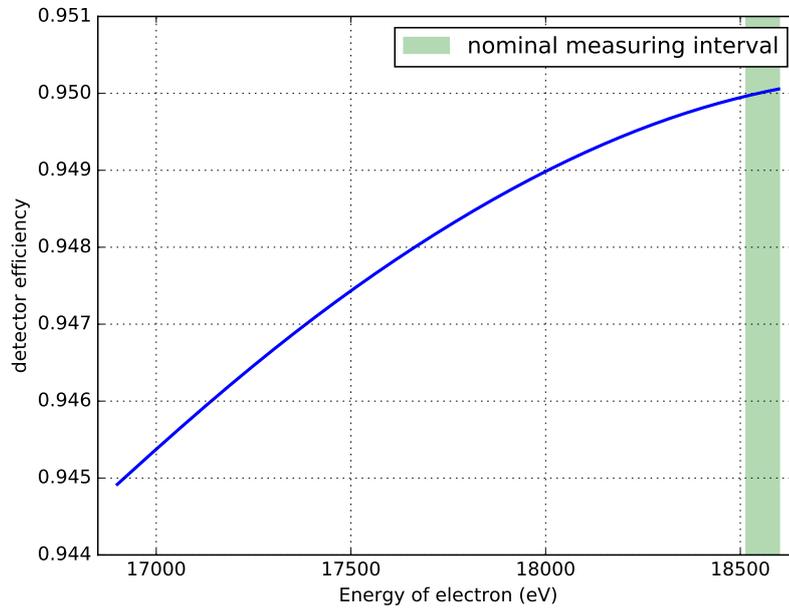
Figure 6.9: Energy dependence of the detector efficiency. In the usual measuring range this effect can be safely neglected. By going deeper in the spectrum the effect becomes noticable.

gun will also bring new insights into this issue. The results of the column density measurement can be compared with the calculated values and might hereby clarify the difference between fit values und calculated values.
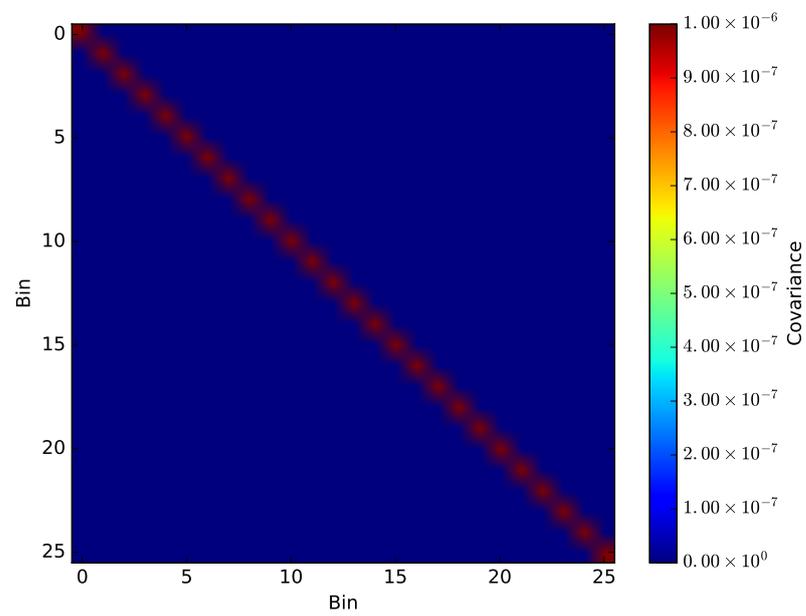
Figure 6.10: The fractional covariance matrix of the DT-fluctuations. Since the fluctuations of the tritium purity are uncorrelated for each measuring point the matrix has just values on its diagonal.
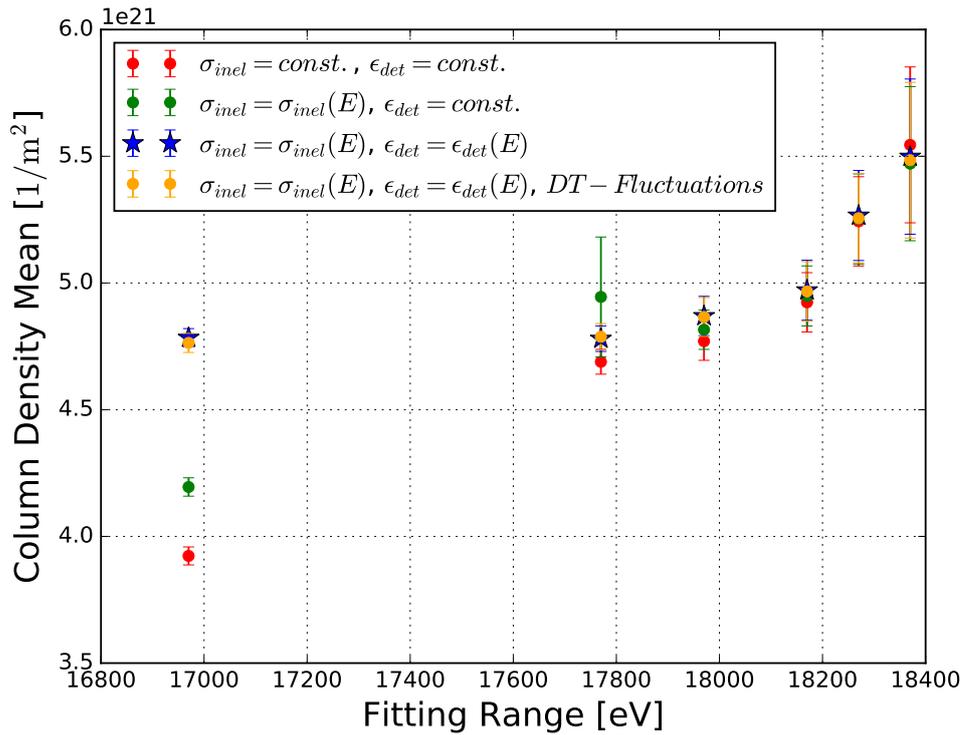
Figure 6.11: The mean value of all column density fits of the 3h runs at different fitting ranges without systematic effects (red), with a energy dependent inelastic cross section (green) with a energy dependent cross section and detector efficiency (blue) and adding a covariance matrix containing fluctuations of the DT concentration (orange).

# Chapter 7

# Conclusions and Outlook

The discovery of neutrino oscillations proved that neutrinos are not massless particles. The current best upper limit for the neutrino mass is at $2 \text{ eV}/c^2$ [7]. The KArlsruhe TRItium Neutrino (KATRIN) experiment targets to push this limit down by one order of magnitude by a model independent investigation of tritium beta decay. For this ambitious goal to be achieved it is of enormous importance to keep the systematic uncertainty as low as possible.

In the first part of this thesis the sensitivity on the squared neutrino mass was examined at different stages of the KATRIN experiment. The three stages that were investigated were the low statistics measurement, the moment at which the sensitivity reaches 1 eV and the full measuring time of 3 years.

A description of all systematic effects that were investigated and their shift of the squared neutrino mass if they are neglected was given. The three systematic effects that create the biggest shifts of the squared neutrino mass if neglected are synchrotron radiation, the thermal doppler effect and a detailed description of the transmission function using a non-isotropic angular distribution of electrons. The shifts of those three effects were compared to the statistical uncertainty at each of the three stages respectively. The outcome shows that for First Tritium the systematic effects have only tiny influence since this measurement is completely dominated by the statistical uncertainty with a rough sensitivity of only $5 \text{ eV}/c^2$ on the neutrino mass. Once the main measurement phase starts the sensitivity of 1 eV is reached after just a bit more than one week of full measuring time. None of the systematic effects has reached a size of 10% of the statistical uncertainty at

that time if considered individually, but the effect coming from the synchrotron radiation reaches this level after about half a month, followed by the doppler effect, which reaches 10% of the statistical uncertainty after about one and a half months of measuring time (see fig. 4.3 and tab. 4.4). For the analysis of the data after the full measuring time of 3 years the statistical uncertainty is quite low ($\sigma_{stat} = 0.0368$ eV$^2$ using a flat MTD in a 60 eV range) and even small effects have influence on the neutrino mass.

As a next step the influence of uncertainties of the control parameters of the experiment were investigated. An accuracy limit for the magnetic fields and the column density could be determined for the three stages of the experiment. The outcome has shown that the required accuracy on the control parameters after three years of measuring time is too stringent if the squared neutrino mass shift induced by the uncertainty of the control parameters is supposed to stay smaller than 10% of the systematic budget. This can be explained by the choice of the measuring time distribution. Taking the column density as an example it was shown that reducing the measuring range from 60 eV to 30 eV below the endpoint decreases the systematic shift significantly. On top of this the measuring time distribution was chosen to be flat for the simulations. Using an optimized MTD improves the result further and the accuracy requirement of the Design Report can be validated.

The second part of this thesis is concerned with the data obtained during the First Tritium campaign. The different methods of fitting were listed and explained. A first look at the data was given, showing fits and results of the Very First Tritium and the First Tritium campaign. It was also shown that there are no correlations between the considered parameters except for the correlation between the normalization and the DT concentration, which could disappear with the new updated run summaries. At last the evolution of the fit parameters over all runs were displayed, showing the stability of the parameters.

Especially the determination of the column density is very important for the First Tritium measurements since the electron gun was not available during this time. The methods that are used to obtain information on the column density from the

data were introduced and the results were compared with the values that were calculated from control parameters that are related to the column density. The comparison shows that only for the runs that were performed at reduced column density the results agree with each other. For the other runs the fitted values were higher than the calculated ones.

Furthermore the fit results showed a strong dependence on the fitting range. This behaviour was expected to be related to systematic effects and an imperfection of the model. Step by step systematic effects were included in the fit. The outcome shows that adding the energy dependent systematic effects of an energy dependent inelastic cross section and an energy dependent detector efficiency reduces the range dependence but it does not disappear completely. Moreover the difference between the calculated values and the fit results remains. In the next steps more systematic effects will be included via a covariance matrix. The ongoing measurements with the electron gun will additionally help resolving this issue.

# Appendix A

# Measuring time distribution tables

Table A.1: Presumed measuring time distribution of the low statistics simulations in the last 200 eV below the endpoint.

| Retarding energy qU (eV) | fraction of measuring time |
|---|---|
| 18375 | 0.015873 |
| 18400 | 0.015873 |
| 18425 | 0.015873 |
| 18450 | 0.015873 |
| 18475 | 0.047619 |
| 18485 | 0.047619 |
| 18495 | 0.047619 |
| 18505 | 0.047619 |
| 18515 | 0.047619 |
| 18525 | 0.047619 |
| 18535 | 0.047619 |
| 18545 | 0.047619 |
| 18555 | 0.063492 |
| 18565 | 0.063492 |
| 18575 | 0.079365 |
| 18585 | 0.079365 |
| 18595 | 0.079365 |
| 18605 | 0.079365 |

Table A.2: Assumed flat MTD settings for the simulations of the full measurement phase. Shown in the table are all measuring points. The fraction of measuring time was 0.015873 at every point.

| Retarding energy qU (eV) | Retarding energy qU (eV) |
| --- | --- |
| -60.0 | -10.0 |
| -57.5 | -9.0 |
| -55.0 | -8.0 |
| -52.5 | -7.75 |
| -50.0 | -7.5 |
| -47.5 | -7.25 |
| -45.0 | -7.0 |
| -42.5 | -6.75 |
| -40.0 | -6.5 |
| -37.5 | -6.25 |
| -35.0 | -6.0 |
| -32.5 | -5.75 |
| -30.0 | -5.5 |
| -29.0 | -5.25 |
| -28.0 | -5.0 |
| -27.0 | -4.75 |
| -26.0 | -4.5 |
| -25.0 | -4.25 |
| -24.0 | -4.0 |
| -23.0 | -3.75 |
| -22.0 | -3.5 |
| -21.0 | -3.25 |
| -20.0 | -3.0 |
| -19.0 | -2.0 |
| -18.0 | -1.0 |
| -17.0 | 0.0 |
| -16.0 | 1.0 |
| -15.0 | 2.0 |
| -14.0 | 3.0 |
| -13.0 | 4.0 |
| -12.0 | 5.0 |
| -11.0 | |

# Bibliography

[1]  PAULI, Wolfgang: Zur älteren und neueren Geschichte des Neutrinos. (German) [On old and new history of the neutrino]. 1961, S. 156–180. – Reprint

[2]  REINES, F. ; COWAN, C. L.: Detection of the Free Neutrino. In: *Phys. Rev.* 92 (1953), Nov, 830–831. `http://dx.doi.org/10.1103/PhysRev.92.8 30`. – DOI 10.1103/PhysRev.92.830

[3]  FUKUDA, Y. et. al.: Evidence for Oscillation of Atmospheric Neutrinos. In: *Phys. Rev. Lett.* 81 (1998), Aug, 1562–1567. `http://dx.doi.org/10.1103/Ph ysRevLett.81.1562`. – DOI 10.1103/PhysRevLett.81.1562

[4]  AHMAD, Q. R. et. al.: Measurement of the Rate of $\nu_e + d \rightarrow p + p + e^-$ Interactions Produced by $^8B$ Solar Neutrinos at the Sudbury Neutrino Observatory. In: *Phys. Rev. Lett.* 87 (2001), Jul, 071301. `http://dx.doi.org/10.1103 /PhysRevLett.87.071301`. – DOI 10.1103/PhysRevLett.87.071301

[5]  KRAUS, C. ; BONN, J. ; BORNSCHEIN, B. ; BORNSCHEIN, L. ; FLATT, B. ; KOVALIK, A. ; MÜLLER, B. ; OTTEN, E.W. ; THÜMMLER, T. ; SCHALL, J.P. ; WEINHEIMER, C.: Latest results of the Mainz Neutrino Mass Experimen. In: *The European Physical Journal C - Particles and Fields* 33 (2004), Jul, Nr. 1, s805–s807. `http://dx.do i.org/10.1140/epjcd/s2003-03-902-9`. – DOI 10.1140/epjcd/s2003– 03–902–9. – ISSN 1434–6052

[6]  LOBASHEV, V.M ; ASEEV, V.N ; BELESEV, A.I ; BERLEV, A.I ; GERASKIN, E.V ; GOLUBEV, A.A ; KAZACHENKO, O.V ; KUZNETSOV, Yu.E ; OSTROUMOV, R.P ; RIVKIS, L.A ; STERN, B.E ; TITOV, N.A ; ZADOROZHNY, S.V ; ZAKHAROV, Yu.I: Direct search for mass of neutrino and anomaly in the tritium beta-spectrum. In: *Physics Letters B* 460 (1999), Nr. 1, 227 - 235. `http://dx.do i.org/https://doi.org/10.1016/S0370-2693(99)00781-9`. – DOI https://doi.org/10.1016/S0370–2693(99)00781–9. – ISSN 0370–2693

[7] AMSLER, C. et. al.: Review of Particle Physics. In: *Physics Letters B* 667 (2008), Nr. 1, 1 - 6. `http://dx.doi.org/https://doi.org/10.1016/j.phy sletb.2008.07.018`. – DOI https://doi.org/10.1016/j.physletb.2008.07.018. – ISSN 0370–2693. – Review of Particle Physics

[8] KATRIN COLLABORATION ; KATRIN COLLABORATION: KATRIN design report 2004 / Forschungszentrum, Karlsruhe. 2005. (Wissenschaftliche Berichte. FZKA). – Forschungsbericht. – ISSN 0947–8620. – 51.54.01; LK 01; Auch: NPI ASCR Rez EXP-01/2005; MS-KP-0501

[9] CHADWICK, J: Intensitätsverteilung im magnetischen Spectrum der $\beta$-Strahlen von radium B + C. In: *Verhandl. Dtsc. Phys. Ges.* 16 (1914), 383. `http://cds.cern.ch/record/262756`

[10] FERMI, E.: An attempt of a theory of beta radiation. 1. In: *Z. Phys.* 88 (1934), S. 161–177. `http://dx.doi.org/10.1007/BF01351864`. – DOI 10.1007/BF01351864

[11] BETHE, H. ; PEIERLS, R.: The 'neutrino'. In: *Nature* 133 (1934), S. 532. `http://dx.doi.org/10.1038/133532a0`. – DOI 10.1038/133532a0

[12] REINES, Frederick ; COWAN, Clyde L.: The neutrino. In: *Nature* 178 (1956), S. 446–449. `http://dx.doi.org/10.1038/178446a0`. – DOI 10.1038/178446a0

[13] DANBY, G. ; GAILLARD, J-M. ; GOULIANOS, K. ; LEDERMAN, L. M. ; MISTRY, N. ; SCHWARTZ, M. ; STEINBERGER, J.: Observation of High-Energy Neutrino Reactions and the Existence of Two Kinds of Neutrinos. In: *Phys. Rev. Lett.* 9 (1962), Jul, 36–44. `http://dx.doi.org/10.1103/PhysRevLett.9.36`. – DOI 10.1103/PhysRevLett.9.36

[14] KODAMA, K. et. al.: Observation of tau neutrino interactions. In: *Physics Letters B* 504 (2001), Nr. 3, 218 - 224. `http://dx.doi.or g/https://doi.org/10.1016/S0370-2693(01)00307-0`. – DOI https://doi.org/10.1016/S0370–2693(01)00307–0. – ISSN 0370–2693

[15] CLEVELAND, Bruce T. ; DAILY, Timothy ; RAYMOND DAVIS, Jr. ; DISTEL, James R. ; LANDE, Kenneth ; LEE, C. K. ; WILDENHAIN, Paul S. ; ULLMAN,

Jack: Measurement of the Solar Electron Neutrino Flux with the Homestake Chlorine Detector. In: *The Astrophysical Journal* 496 (1998), Nr. 1, 505. `http://stacks.iop.org/0004-637X/496/i=1/a=505`

[16] BILENKY, Samoil M. ; PONTECORVO, B.: Lepton Mixing and Neutrino Oscillations. In: *Phys. Rept.* 41 (1978), S. 225–261. `http://dx.doi.org/10.10 16/0370-1573(78)90095-9`. – DOI 10.1016/0370–1573(78)90095–9

[17] PONTECORVO, B.: Neutrino Experiments and the Problem of Conservation of Leptonic Charge. In: *Sov. Phys. JETP* 26 (1968), S. 984–988. – [Zh. Eksp. Teor. Fiz.53,1717(1967)]

[18] GRIBOV, V. ; PONTECORVO, B.: Neutrino astronomy and lepton charge. In: *Physics Letters B* 28 (1969), Nr. 7, 493 - 496. `http://dx.doi. org/https://doi.org/10.1016/0370-2693(69)90525-5`. – DOI https://doi.org/10.1016/0370–2693(69)90525–5. – ISSN 0370–2693

[19] MAKI, Ziro ; NAKAGAWA, Masami ; SAKATA, Shoichi: Remarks on the Unified Model of Elementary Particles. In: *Progress of Theoretical Physics* 28 (1962), Nr. 5, 870-880. `http://dx.doi.org/10.1143/PTP.28.870`. – DOI 10.1143/PTP.28.870

[20] AHMAD, Q. R. et. al.: Direct Evidence for Neutrino Flavor Transformation from Neutral-Current Interactions in the Sudbury Neutrino Observatory. In: *Phys. Rev. Lett.* 89 (2002), Jun, 011301. `http://dx.doi.org/10.1103/PhysRe vLett.89.011301`. – DOI 10.1103/PhysRevLett.89.011301

[21] TANABASHI, M. et. al.: Review of Particle Physics. In: *Phys. Rev. D* 98 (2018), Aug, 030001. `http://dx.doi.org/10.1103/PhysRevD.98.030001`. – DOI 10.1103/PhysRevD.98.030001

[22] LESGOURGUES, Julien ; PASTOR, Sergio: Neutrino mass from Cosmology. In: *Adv. High Energy Phys.* 2012 (2012), S. 608515. `http://dx.doi.org/10. 1155/2012/608515`. – DOI 10.1155/2012/608515

[23] VOGEL, Petr: Neutrinoless double beta decay. In: *Proceedings of Theoretical Advanced Study Institute in Elementary Particle Physics : Exploring New Frontiers*

*Using Colliders and Neutrinos (TASI 2006): Boulder, Colorado, June 4-30, 2006*, 2006, S. 577–608

[24] ALBERT, J. B. et. al.: Search for Majorana neutrinos with the first two years of EXO-200 data. In: *Nature* 510 (2014), S. 229–234. `http://dx.doi.org/1 0.1038/nature13432`. – DOI 10.1038/nature13432

[25] BETTINI, A.: GERDA. Germanium Detector Array. Search for Neutrino-less double beta Decay of 76Ge. In: *Nuclear Physics B - Proceedings Supplements* 168 (2007), 67 - 69. `http://dx.doi.org/htt ps://doi.org/10.1016/j.nuclphysbps.2007.02.018`. – DOI https://doi.org/10.1016/j.nuclphysbps.2007.02.018. – ISSN 0920–5632. – Proceedings of the Neutrino Oscillation Workshop

[26] AALSETH, C. E. et. al.: The Majorana Ge-76 double beta decay project. In: *Nonaccelerator new physics. Proceedings, 3rd International Conference, NANP 2001, Dubna, Russia, June 19-32, 2001*, 2002

[27] ARTUSA, D. R. et. al.: Searching for neutrinoless double-beta decay of $^{130}$Te with CUORE. In: *Adv. High Energy Phys.* 2015 (2015), S. 879871. `http: //dx.doi.org/10.1155/2015/879871`. – DOI 10.1155/2015/879871

[28] GANDO, A. et. al.: Search for Majorana Neutrinos near the Inverted Mass Hierarchy Region with KamLAND-Zen. In: *Phys. Rev. Lett.* 117 (2016), Nr. 8, S. 082503. `http://dx.doi.org/10.1103/PhysRevLett.117.1 09903,10.1103/PhysRevLett.117.082503`. – DOI 10.1103/PhysRev-Lett.117.109903, 10.1103/PhysRevLett.117.082503. – [Addendum: Phys. Rev. Lett.117,no.10,109903(2016)]

[29] OSIPOWICZ, A. et. al.: KATRIN: A Next generation tritium beta decay experiment with sub-eV sensitivity for the electron neutrino mass. Letter of intent. (2001)

[30] FAVERZANI, M. et. al.: The HOLMES Experiment. In: *Journal of Low Temperature Physics* 184 (2016), Aug, Nr. 3, 922–929. `http://dx.doi.org/10.1007/s 10909-016-1540-x`. – DOI 10.1007/s10909–016–1540–x. – ISSN 1573–7357

[31] GASTALDO, L. et. al.: The Electron Capture $^{163}$Ho Experiment ECHo. In: *Journal of Low Temperature Physics* 176 (2014), Sep, Nr. 5, 876–884. `http://dx.doi.org/10.1007/s10909-014-1187-4`. – DOI 10.1007/s10909–014–1187–4. – ISSN 1573–7357

[32] NUCCIOTTI, A. ; ARNABOLDI, C. ; BROFFERIO, C. ; CREMONESI, O. ; FIORINI, E. ; GIULIANI, A. ; MARGESIN, B. ; MARTENSSON, L. ; PAVAN, M. ; PESSINA, G. ; PIRRO, S. ; PREVITALI, E. ; SISTI, M. ; ZEN, M.: The Milano neutrino mass experiment with arrays of AgReO4 microcalorimeters. In: *AIP Conference Proceedings* 605 (2002), Nr. 1, 453-456. `http://dx.doi.org/10.1063/1.1457684`. – DOI 10.1063/1.1457684

[33] NUCCIOTTI, A.: Neutrino mass calorimetric searches in the MARE experiment. In: *Nucl. Phys. Proc. Suppl.* 229-232 (2012), S. 155–159. `http://dx.doi.org/10.1016/j.nuclphysbps.2012.09.025`. – DOI 10.1016/j.nuclphysbps.2012.09.025

[34] ESFAHANI, Ali A. et. al.: Determining the neutrino mass with cyclotron radiation emission spectroscopy—Project 8. In: *Journal of Physics G: Nuclear and Particle Physics* 44 (2017), Nr. 5, 054004. `http://stacks.iop.org/0954-3899/44/i=5/a=054004`

[35] AMSBAUGH, J. F. et. al.: Focal-plane detector system for the KATRIN experiment. In: *Nucl. Instrum. Meth.* A778 (2015), S. 40–60. `http://dx.doi.org/10.1016/j.nima.2014.12.116`. – DOI 10.1016/j.nima.2014.12.116

[36] BECK, M. et. al.: An angular-selective electron source for the KATRIN experiment. In: *JINST* 9 (2014), Nr. 11, S. P11020. `http://dx.doi.org/10.1088/1748-0221/9/11/P11020`. – DOI 10.1088/1748–0221/9/11/P11020

[37] VALERIUS, K. et. al.: Prototype of an angular-selective photoelectron calibration source for the KATRIN experiment. In: *JINST* 6 (2011), S. P01002. `http://dx.doi.org/10.1088/1748-0221/6/01/P01002`. – DOI 10.1088/1748–0221/6/01/P01002

[38] STEINBRINK, Nicholas ; HANNEN, Volker ; MARTIN, Eric L. ; ROBERTSON, R. G. H. ; ZACHER, Michael ; WEINHEIMER, Christian: Neutrino mass sensitivity

by MAC-E-Filter based time-of-flight spectroscopy with the example of KAT-RIN. In: *New J. Phys.* 15 (2013), S. 113020. `http://dx.doi.org/10.1088/1367-2630/15/11/113020`. – DOI 10.1088/1367–2630/15/11/113020

[39] KLEESIEK, Marco: *A Data-Analysis and Sensitivity-Optimization Framework for the KATRIN Experiment*, Karlsruhe U., EKP, Diss., 2014. `http://primo.bibliothek.kit.edu/primo_library/libweb/action/dlDisplay.do?vid=KIT&docId=KITSRCE1000043301&tab=kit_evastar&srt=date`

[40] KLEESIEK, M. et. al.: $\beta$-Decay Spectrum, Response Function and Statistical Model for Neutrino Mass Measurements with the KATRIN Experiment. (2018)

[41] KARL, Christian: *Analysis of First Tritium Data of the KATRIN Experiment.* 2018

[42] BEHRENS, Jan: *Neutrino mass sensitivity studies.* `https://neutrino.ikp.kit.edu/katrin/images/3/31/MtdWorkshop_20181018.pdf`. – KATRIN MTD Workshop 2018

[43] FISCHER, S. ; STURM, M. ; SCHLÖSSER, M. ; LEWIS, R.J. ; BORNSCHEIN, B. ; DREXLIN, G. ; TELLE, H.H.: Laser Raman Spectroscopy for KATRIN. In: *Nuclear Physics B - Proceedings Supplements* 229-232 (2012), 492. `http://dx.doi.org/https://doi.org/10.1016/j.nuclphysbps.2012.09.129`. – DOI https://doi.org/10.1016/j.nuclphysbps.2012.09.129. – ISSN 0920–5632. – Neutrino 2010

[44] HEIZMANN, Florian: *Calculations of column densities from throughput, RunSummary etc..* `https://neutrino.ikp.kit.edu/katrin/images/8/89/2018-07-19-ThroughputColdensETC.pdf`. – KATRIN Analysis Workshop 2018

[45] LIU, J. W.: Total Inelastic Cross Section for Collisions of $H_2$ with Fast Charged Particles. In: *Phys. Rev. A* 7 (1973), Jan, 103–109. `http://dx.doi.org/10.1103/PhysRevA.7.103`. – DOI 10.1103/PhysRevA.7.103

[46] ENOMOTO, Sanshiro ; KORZECZEK, Marc: *Detection Efficiencies for First Tritium.* `https://neutrino.ikp.kit.edu/katrin/images/c/cc/DetectionEfficiencyPreliminary-20180720v2.pdf`. – KATRIN Analysis Workshop 2018

[47] SCHLÖSSER, Magnus: *First Tritium data.* `https://neutrino.ikp.ki t.edu/ katrin/ images/ d/ d9/ 180716-KATRIN-Muenchen-MSchloe sser.pptx.` – KATRIN Analysis Workshop 2018

# Acknowledgements

At this point i just want express my gratitude that i was given the chance to be part of the KATRIN collaboration and to thank all the people that supported me during this time. Special thanks go to:

- Prof. Dr. Susanne Mertens for giving me the opportunity to work on this thesis and for her excellent supervision, always being very patient. In general it was very pleasant to work in her group. Also thanks for always supporting and encouraging me in extending my skills and learning new things. I also want to thank her for guiding me through and correcting my thesis.

- Dr. Thierry Lasserre for the many discussions, for always being helpful answering questions and his experienced view on my results, giving tips on how to proceed further.

- Dr. Martin Slezák for his patient help at C++ or general programming issues, which was always very valuable and for solving many general computing problems. I also want to thank him for his effort in proofreading this thesis and that he was always available for questions and helping with competent answers.

- Dr. Wonqook Choi and Moritz Machatschek for their help with SSC and KaFit problems.

- Christian Karl for always helping me with programming problems. For encouraging me to improve my computer skills and for his valuable tips that facilitated my work. Also for always being available for questions about Fitrium.

- The whole Munich KATRIN Group for the good working atmosphere and the many activities in and outside of work that made this time so special. Also for

the many physics discussions that helped to deepen my understanding of the KATRIN experiment and of neutrino physics in general and for giving tips on how to improve my work.

- My Family and Friends for giving me balance and supporting me not only during this thesis but also in every other aspect.